

# The dynamic structure underlying subthreshold oscillatory activity and the onset of spikes in a model of medial entorhinal cortex stellate cells

Horacio G. Rotstein · Tim Oppermann ·  
John A. White · Nancy Kopell

Received: 16 February 2005 / Revised: 26 February 2006 / Accepted: 1 March 2006 / Published online: 14 August 2006  
© Springer Science + Business Media, LLC 2006

**Abstract** Medial entorhinal cortex layer II stellate cells display subthreshold oscillations (STOs). We study a single compartment biophysical model of such cells which qualitatively reproduces these STOs. We argue that in the subthreshold interval (STI) the seven-dimensional model can be reduced to a three-dimensional system of equations with well differentiated times scales. Using dynamical systems arguments we provide a mechanism for generations of STOs. This mechanism is based on the “canard structure,” in which relevant trajectories stay close to repelling manifolds for a significant interval of time. We also show that the transition from subthreshold oscillatory activity to spiking (“canard explosion”) is controlled in the STI by the same structure. A similar mechanism is invoked to explain why noise increases the robustness of the STO regime. Taking advantage of the reduction of the dimensionality of the full stellate cell system, we propose a nonlinear artificially spiking (NAS) model in which the STI reduced system is supplemented with a threshold for spiking and a reset voltage. We show that the synchronization properties in networks made up of

the NAS cells are similar to those of networks using the full stellate cell models.

**Keywords** Theta rhythm · Reduction of dimensions · Hopf bifurcation · Canard · Generalized integrate-and-fire models

## 1. Introduction

The flow of information from the neocortex to the hippocampus is orchestrated by the superficial cell layers (II and III) of the entorhinal cortex (EC). The spiny stellate cells (SCs) of Ramon y Cajal constitute the most abundant principal cell type in layer II of the medial EC (MEC) and these neurons give rise to the perforant path, the main afferent fiber system to the hippocampus. *In vivo* electrophysiological investigations have shown that the MEC generates rhythmic activity at theta frequencies (8–12 Hz), and that the firing of MEC layer II (MEC-II) neurons is highly phase locked to the theta field events (Alonso and García, 1987). Many lines of evidence indicate that the theta rhythm is implicated in learning and memory processes (Winston, 1978; Buzsáki, 1989; Kahana et al., 1999), one of the main functions of the medial temporal lobe of which the EC is a crucial component. Importantly, *in vitro* electrophysiological studies have also established that the SCs develop low-amplitude (1–4 mV) rhythmic subthreshold membrane potential oscillations (STOs) at theta frequencies; when the membrane potential is set positive to threshold (about  $-50$  mV), SCs fire action potentials at the peak of the STO but not necessarily at every STO’s cycle (Dickson et al., 2000b). Mixed-mode oscillatory (MMO) activity, the coexistence of spiking and subthreshold oscillations, is a distinctive property of SCs *in vitro*. Notably, the firing of MEC layer II neurons has also

---

In memory of Angel A. Alonso

---

H. G. Rotstein (✉) · N. Kopell  
Department of Mathematics and Center for Biodynamics,  
Boston University, Boston, MA 02215, USA

T. Oppermann  
Institute for Theoretical Biology, Humboldt University Berlin,  
10115 Berlin, Germany

J. A. White  
Department of Biomedical Engineering and Center for  
Biodynamics, Boston University,  
Boston, MA 02215, USA

been shown to skip theta cycles *in vivo* (Alonso and García Austt, 1987).

Theta STOs in SCs are intrinsic single cell phenomena, which persist during synaptic transmission block, as originally demonstrated by Alonso and Llinás (1989). The persistent sodium ( $I_{\text{Nap}}$ ) and  $h$ -( $I_h$ ) currents have been implicated in the pacemaking of single-cell rhythmicity at theta frequencies (Alonso and Llinás, 1989; Alonso and Klink, 1993; Klink and Alonso, 1993, 1997; Magistretti and Alonso, 1999; Magistretti and Ragsdale, 1999; Dickson et al., 2000a, b; Gillies et al., 2002; Fransén et al., 2004; Rotstein et al., 2005b) (see also references therein). The former constitutes a depolarization-activated fast inward current that provides the main drive for the depolarizing phase of the STOs. The latter, which is a hyperpolarization-activated non-inactivating current with slow kinetics, provides a delayed feedback effect that promotes resonance. Theoretical studies, based on simulations of biophysical models, have shown that the interplay between  $I_h$  and  $I_{\text{Nap}}$  may be sufficient to account for the generation of membrane potential oscillations in MEC-II SCs (Dickson et al., 2000a, b; Fransén et al., 1998, 1999, 2004; White et al., 1995, 1998). However, the dynamic mechanism governing this interaction has not yet been explored.

The goal of this paper is to explain the dynamic mechanism governing the generation of STOs, spikes and MMOs in a conductance based model of MEC-II SCs that was introduced by Acker et al. (2003) to study the synchronization properties of SC networks. We describe that model in Section 2. It incorporates a  $I_{\text{Nap}}$  and a two-component (fast and slow)  $I_h$  in addition to the standard sodium ( $I_{\text{Na}}$ ), potassium ( $I_{\text{K}}$ ) and leak ( $I_{\text{L}}$ ) Hodgkin-Huxley (HH) currents.

We use reduction of dimensions arguments, not all standard (see Section 3.2), to uncover a three-dimensional regime (called the STO regime) whose dynamic structure governs the generation of STOs and MMOs. More specifically, we argue that, during the largest part of the subthreshold interval (STI),  $I_{\text{Na}}$  and  $I_{\text{K}}$  are inactive (much smaller than the other participating currents, and such that taking them away does not change the dynamic structure of the problem), leaving  $I_{\text{L}}$ ,  $I_{\text{Nap}}$ ,  $I_h$  (with its slow and fast components  $I_{h_f}$  and  $I_{h_s}$ ) as the only active currents. In addition, the  $I_{\text{Nap}}$  gating variable  $p$  evolves on a much faster time scale than the rest of the remaining variables, so  $p$  is slaved to the voltage. Even though  $p$  is also a small current in the STO regime, we find that  $I_{\text{Nap}}$  cannot be eliminated for the relevant range of parameters considered. The essential aspects of the dynamics of the SC during the STI can be captured by a reduced three-dimensional system of differential equations, which describes the evolution of the voltage and the two  $I_h$ , fast ( $r_f$ ) and slow ( $r_s$ ), gating variables. The study of the SC dynamics in the STO regime is further simplified by the fact that  $I_h$  resets during a spike (occurring in a prior regime),

setting the initial conditions for the corresponding  $I_h$  gating variables very close to zero, and allowing one to study only the trajectories starting in a restricted domain.

In the STO regime one can describe the onset of a spike but not the spiking dynamics. This can be studied using classical techniques (Rinzel, 1985; Koch, 1999).

At the heart of the mechanism of generation of STOs and MMOs is a phenomenon associated with the geometry of invariant manifolds when there are multiple times scales. When an invariant manifold is unstable, in general trajectories starting near it quickly move away from it. However, if the invariant manifold is associated with slower motion, there are circumstances in which the trajectories starting adequately nearby can stay near the invariant manifold for a significant amount of time before escaping in the direction of another (stable) manifold. STOs are produced when the latter invariant manifold is close enough and causes the trajectory to move backwards towards it. A prototypical example of this type of behavior are the oscillations around the knee of a parabolic manifold with one stable and one unstable branch. In two-dimensional systems, this is associated with the canard phenomenon (canard explosion), a sudden increase in the amplitude of the limit cycle (stable or unstable) created in a Hopf-bifurcation as some parameter is changed (Benoit et al., 1980; Eckhaus, 1983; Dumortier and Roussarie, 1996; Krupa and Szmolyan, 2001). In 2D, the system may display either STOs or large amplitude relaxation oscillations (spikes), but never both. The canard phenomenon in three-dimensional systems is more generic and MMOs are possible provided an adequate return mechanism that brings these variables back to their initial conditions in the STO regime (Szmolyan and Wechselberger, 2001; Wechselberger, 2005; Brons et al., 2005).

The geometric/dynamic structure generated by the null-surfaces and time scale separation in the 3D reduced system is called the “canard structure” and has the potential to produce canard solutions and the canard explosion (in the form of STOs and MMOs). The key feature, as mentioned above, is the existence of trajectories that follow an unstable manifold for a significant amount of time. The canard structure we have in mind is created by the 3D system of (fast) voltage and (slow)  $I_h$  gating variables ( $r_f$  and  $r_s$ ). The nonlinearities associated with the slow manifold are locally “parabolic”: the nullsurface is an inverted cylindrical paraboloid whose folded line (curve of knees) has positive ( $V, r_f, r_s$ ) coordinates. For the specific model we use, the spike in a prior regime resets both  $r_f$  and  $r_s$ , i.e., it plays the role of a return mechanism to the STO regime. More specifically, spikes bring the trajectory to its initial point ( $r_f = r_s = 0$ ) in the STO regime, on the left (stable) branch of the slow manifold. This trajectory then moves fast towards the slow manifold. Initially,  $r_f$  and  $r_s$  evolve with a marked difference in speed, though not an order of magnitude time scale separation. The slow component of

$I_h$  is responsible for bringing back the system from its reset to its STO/MMO values. As this happens the speed separation between  $r_f$  and  $r_s$  decreases. When the trajectory is close to the curve of knees, the overall time separation breaks down.

The subthreshold oscillatory activity seen in experiments is much less regular than the one created by the full SC model (and seen in the reduced three-dimensional model in the STO regime) for the set of parameters considered here. We make use of the stochastic nature of the  $I_{Nap}$  channels (White et al., 1998; Shalinsky et al., 2002) to show voltage traces qualitatively similar (in irregularity and frequency) to experimentally found ones (Dickson et al., 2000a). The effect of noise on the occurrence of STOs can be heuristically explained using the canard structure as a theoretical framework.

The canard structure describes the SC dynamics during most of the STI, including the onset of spikes. One important and useful consequence of our results is that, if one is not interested in the spike details, the dynamics of the SC can be approximately described by the reduced three-dimensional system mentioned above, supplemented with an artificial spike. This simplified model is called nonlinear artificially spiking (NAS) SC model.

The two main differences between these and classical integrate- and resonate-and-fire models (IF or RF) (Izhikevich, 2001) are the mathematical description of the onset of spikes and the return mechanism to the STO region (curve of knees), after a spike. In IF or RF models, these are described by imposing an artificial voltage threshold for spike generation and a reset value after a spike. In the NAS model the onset of spikes is a consequence of the underlying canard structure (canard phenomenon), and the return mechanism is a consequence of the  $h$ -current reset and the time scale separation. The NAS SC model approach has a wider applicability than the description of single cell dynamics. In Appendix B we compare synchronization properties for networks of SCs using both the full and the NAS SC models.

## 2. Methods

The single compartment biophysical model we study here was introduced by Acker et al. (2003) and is based on measurements from layer II SCs of the medial entorhinal cortex (MEC) (White et al., 1995; 1998; Dickson et al., 2000b; Fransén et al., 2004). It has a persistent sodium ( $I_{Nap}$ ) and a two-component (fast and slow) hyperpolarization-activated ( $I_h$ ) currents in addition to the standard Hodgkin-Huxley sodium ( $I_{Na}$ ), potassium ( $I_K$ ) and leak ( $I_L$ ) currents. The current-balance equation is

$$C \frac{dV}{dt} = I_{app} - I_{Na} - I_K - I_L - I_h - I_{Nap} \tag{1}$$

where  $V$  is the membrane potential (mV),  $C$  is the membrane capacitance ( $\mu\text{F}/\text{cm}^2$ ),  $I_{app}$  is the applied bias (DC) current ( $\mu\text{A}/\text{cm}^2$ ),  $I_{Na} = G_{Na} m^3 h (V - E_{Na})$ ,  $I_K = G_K n^4 (V - E_K)$ ,  $I_L = G_L (V - E_L)$ ,  $I_{Nap} = G_p p (V - E_{Na})$ ,  $I_h = G_h (0.65 r_f + 0.35 r_s) (V - E_h)$ .  $G_X$  and  $E_X$  ( $X = Na, K, L, p, h$ ) are the maximal conductances ( $\text{mS}/\text{cm}^2$ ) and reversal potentials (mV) respectively. The units of time are msec. All the gating variables  $x$  ( $x = m, h, n, p, r_f, r_s$ ) obey a first order differential equation of the following form:

$$\frac{dx}{dt} = \frac{x_\infty(V) - x}{\tau_x(V)}, \tag{2}$$

where

$$x_\infty(V) = \frac{\alpha_x(V)}{\alpha_x(V) + \beta_x(V)} \text{ and } \tau_x(V) = \frac{1}{\alpha_x(V) + \beta_x(V)}. \tag{3}$$

The definitions of  $\alpha_x$  and  $\beta_x$  for  $x = m, h, n, p, r_f, r_s$  are given in Appendix A and the corresponding graphs are shown in Fig. 1. The values of the parameters used by Acker et al. (2003) are:  $E_{Na} = 55$ ,  $E_K = -90$ ,  $E_L = -65$ ,  $E_h = -20$ ,  $G_{Na} = 52$ ,  $G_K = 11$ ,  $G_L = 0.5$ ,  $G_p = 0.5$ ,  $G_h = 1.5$  and  $C = 1$ .

Simulations were performed using the modified Euler method and a Runge-Kutta method of order IV (Burden and Faires, 1980).

## 3. Results

### 3.1. Full model: Coexistence of subthreshold oscillations and spikes

In Fig. 2 we present simulation results for the full SC model for various values of  $I_{app}$ . The voltage traces are shown in the two top panels (note that the second panel is a blow-up of the top panel); the  $I_h$  and  $I_{Nap}$  traces are given in the two bottom panels. As the value of  $I_{app}$  increases, the spiking frequency also increases, while the number of STOs per STI decreases and finally vanishes as shown in Fig. 2(d). In all simulations we have done we found that, for relevant initial conditions, voltage traces either display STOs and spikes, or decay to a fixed point in an oscillatory way. In most cases, STOs increase their amplitude as the SC trajectory approaches spiking.

Our results demonstrating the coexistence of STOs and spikes are consistent with experimental findings (Dickson et al., 2000b). However, the STOs predicted using the deterministic full SC model are less robust than experimentally found; i.e., the ratio STO/spikes is larger in experiments than

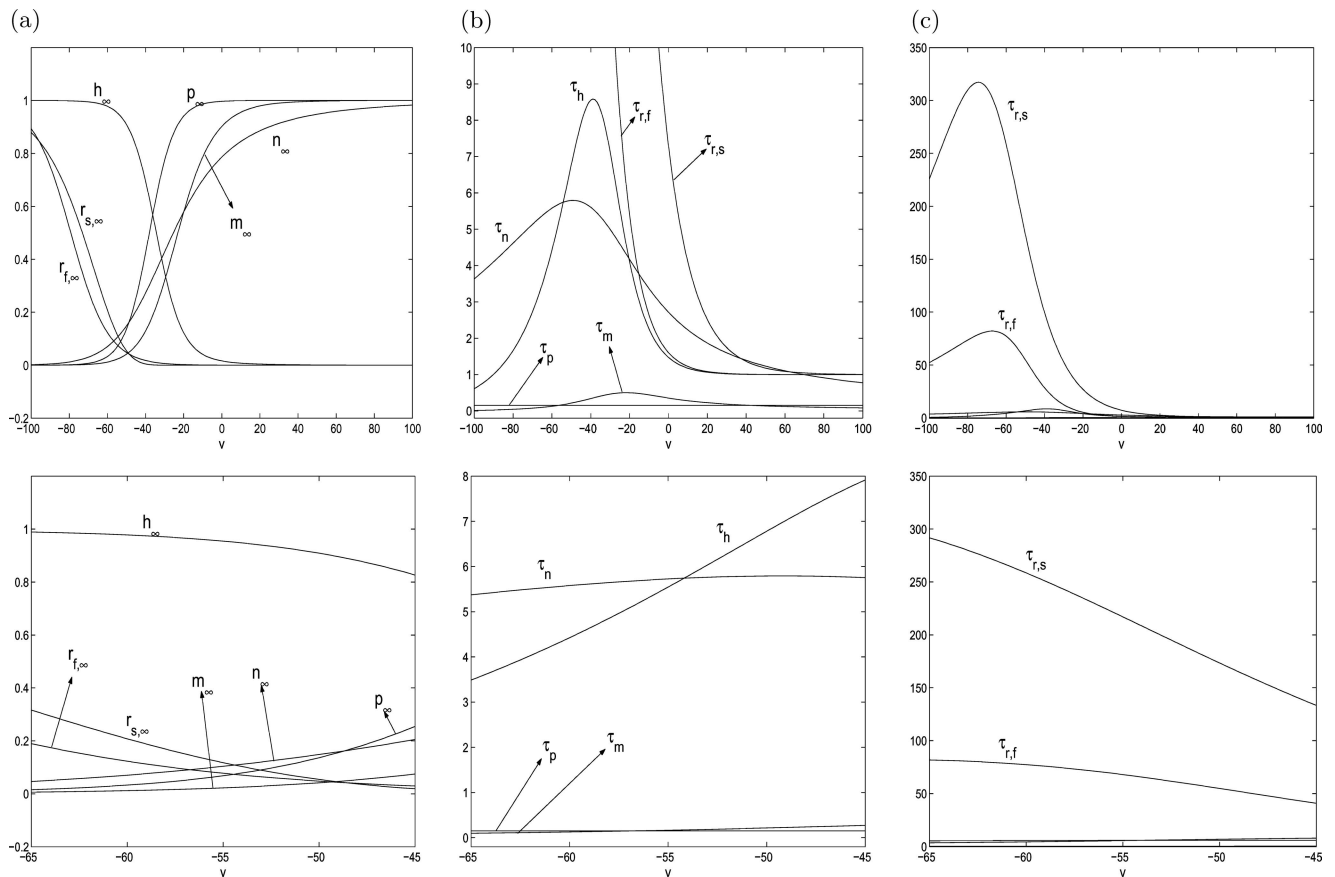


**Fig. 1** Ion channel dynamics for the full SC model (1)–(3). The gating variables are  $x = m, n, h, p, r_f, r_s$ . The bottom panels are magnifications of the top ones. Voltage units are mV. (a) Activation and inactivation curves ( $x_\infty(V)$ ) for the gating variables. (b) Voltage-dependent

time scales ( $\tau_x(V)$ ) for the gating variables. The separation of time-scales is clearly visible. Both  $\tau_{r,f}$  and  $\tau_{r,s}$  evolve on time scales much slower than the other variables. (c) Voltage dependent time scales in a larger time interval.

in simulations. In Section 3.4 we explain how noise is able to correct for this.

Note that, as experimentally found (Dickson et al., 2000a),  $I_{\text{Nap}}$  is at a minimum at the trough of a STO, and  $I_h$  reaches its maximum at the beginning of the depolarizing phase. As depolarization proceeds,  $I_{\text{Nap}}$  rapidly increases, boosting the depolarization initiated by  $I_h$ , which in itself causes the voltage trajectory to reverse to repolarization. Just after the peak of the oscillation,  $I_h$  reaches its minimum.

### 3.2. A reduced SC model valid during the STI

Here we argue that, during the STI,  $I_{\text{Na}}$  and  $I_{\text{K}}$  are almost inactive, leaving  $I_{\text{Nap}}$ ,  $I_h$  and  $I_L$  as the main active currents. We also show that  $p \sim p_\infty(V)$ , so the dynamics of the SC can be approximated by a three-dimensional system describing  $V$ ,  $r_f$  and  $r_s$ . Good approximations for the resulting reduced system initial conditions are obtained from the spike reset of the  $h$ -current as we explain below.

The reduction of dimensions ideas we use to arrive to the reduced equations in the STO regime are not wholly

standard. They include (i) identifying a number of reduced regimes (corresponding to a sequence of subintervals of the cell spiking period), of which the STO is the central one in our study; (ii) identifying the corresponding time scales for each regime; (iii) identifying the “inactive currents” in each regime; i.e., those currents that can be removed from the full system without changing its dynamic features (fixed points and their stability, bifurcation structure, etc.); (iv) identifying the variables that govern the dynamics of the reduced system and the variables that evolve slowly (modulatory); (v) checking that the reduced systems obtained are a good (asymptotic) approximation of the full and giving estimates for the errors made in the approximation; and (vi) giving estimates for the length of the time interval of validity of each one of the reduced regimes. The mathematical formalization of these ideas will be given elsewhere, along with more mathematical details about the bifurcation structure associated with the reduced model using the theory developed by Wechselberger (2005). Here we present our arguments in a heuristic way. Some of the reduction of dimensions ideas discussed here have been used in a computational tool

designed to reduce the dimensionality of neural systems (Clewley et al., 2005).

3.2.1. Reduced equations

Looking at the second panels in Fig. 2 we see that during most of the STI the voltage is bounded between  $-60$  mV and  $-50$  mV. In Figs. 1(b) and (c) (the bottom panels are a blow-up of the top ones), we see that for this interval of values of the voltage,  $\tau_p$ ,  $\tau_m$  and  $\tau_n$  are much smaller than  $\tau_{r_f}$ , which we take as a reference time scale. In addition, from Fig. 1(a),  $m_\infty \sim 0$  and  $n_\infty^4 \sim 0$ . Then  $m \sim 0$ ,  $I_{Na} \sim 0$ ,  $I_K \sim 0$  and  $p \sim p_\infty(v)$ . Thus, we get the following system of equations to approximately describe the dynamics of the SC model during the STI:

$$C \frac{dV}{dt} = I_{app} - G_p p_\infty(V)(V - E_{Na}) - I_L - I_h, \quad (4)$$

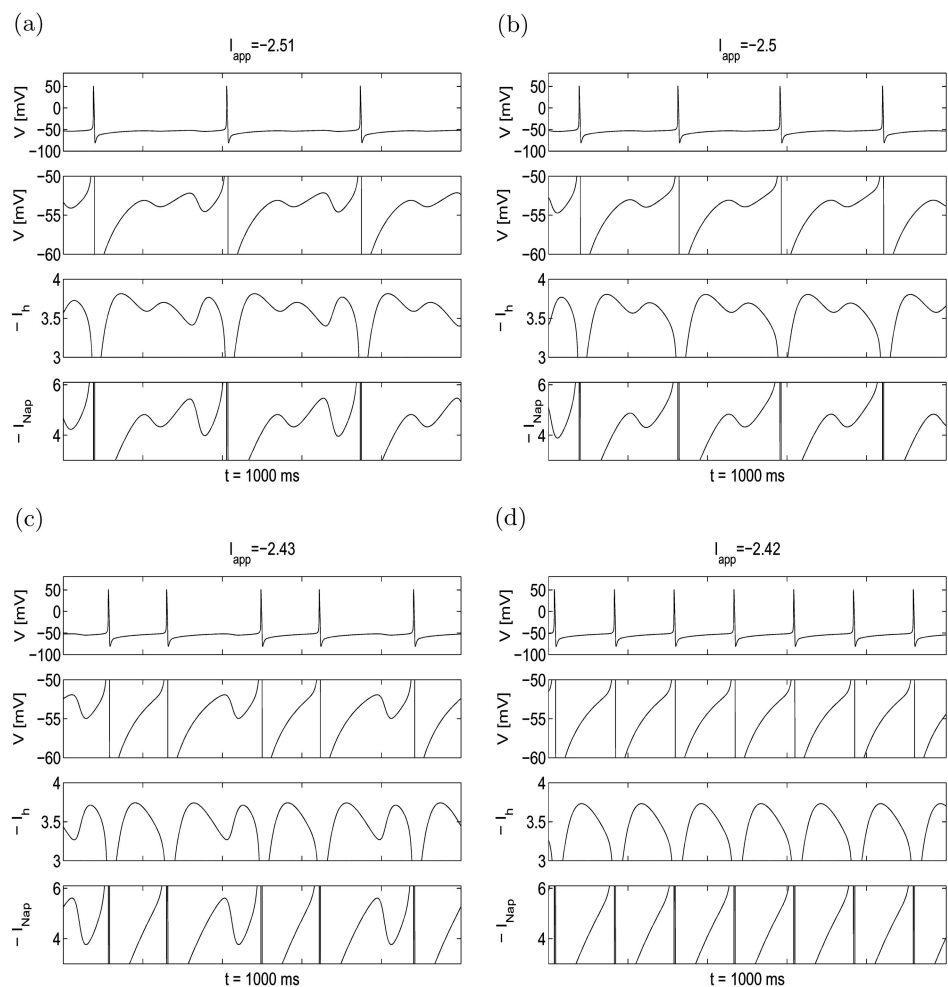
$$\frac{dr_f}{dt} = \frac{r_{f,\infty}(V) - r_f}{\tau_{r_f}(V)}. \quad (5)$$

$$\frac{dr_s}{dt} = \frac{r_{s,\infty}(V) - r_s}{\tau_{r_s}(V)}. \quad (6)$$

As in Eq. (1),  $I_h = G_h(0.65 r_f + 0.35 r_s)(V - E_h)$  and  $I_L = G_L(V - E_L)$ . For future use we call  $I_{h_f} = G_h 0.65 r_f(V - E_h)$  and  $I_{h_s} = G_h 0.35 r_s(V - E_h)$ . Our simulations with the full SC model (1)–(3) show (data not presented here) that  $I_{Na} < I_{h_s}$  during the STO regime.

As part of our study, we checked that removing  $I_{Na}$  and  $I_K$  does not change the dynamic structure (fixed points, stability and bifurcations) of the reduced system as compared to the full one (1–2). This is not ensured by the fact that both currents are very small. Indeed, in a related system studied by Jalics et al. (2005) involving a slow potassium current instead of  $I_h$  (Acker et al., 2003), removing  $I_{Na}$  changes the Hopf bifurcation criticality of the resulting reduced system.

**Fig. 2** Full SC model: Changing  $I_{app}$  changes the ratio of spikes to STOs. Voltage ( $V$ ) traces,  $I_h$  and  $I_{Na}$  for various values of the applied current  $I_{app}$  and  $G_h = 1.5$ . The values of the other parameters used in the simulations are given Section 2. The second row in each panel is a magnification of the first row.



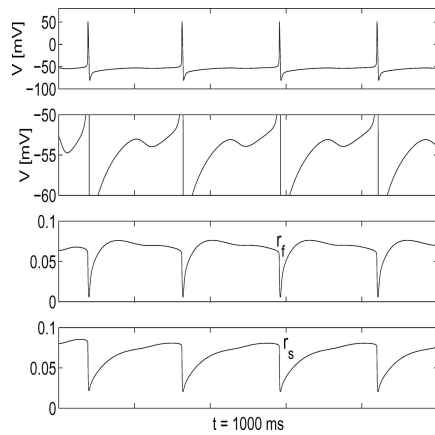


**Fig. 3** Full SC model: Evolution of the voltage ( $V$ ) and  $h$ -current gating variables ( $r_f$  and  $r_s$ ) during STOs and spikes for  $I_{app} = -2.5$  and  $G_h = 1.5$ . The values of the other parameters used in the simulations are given in Section 2. The second row is a magnification of the first row.

One could describe the STO regime as the interval of time for which  $I_{Na}$  and  $I_K$  are inactive in the sense that they are much smaller than  $I_h$ ,  $I_{Nap}$  and  $I_L$ . The voltage bounds during the STI change with different values of  $I_{app}$  and  $G_h$ . However, the reduction of dimensions argument used before remains valid over a large range of these parameters.

### 3.2.2. Reset of $I_h$

The behavior of  $v$ ,  $r_f$  and  $r_s$  are illustrated in Fig. 3. (The second panel is a blow-up of the first.) During a spike,  $v$  increases above zero to a value  $\sim 50$  mV. For these values of  $v$ ,  $r_{f,\infty}(v) \sim 0$  and  $r_{s,\infty}(v) \sim 0$  (see Fig. 1(a)). In addition, for these high values of  $v$ , both  $\tau_{r_f}(v)$  and  $\tau_{r_s}(v)$  are very small (see Fig. 1(b) and (c)), and then both  $r_f$  and  $r_s$  quickly decrease to values close to  $r_f \sim r_s \sim 0$ . In our approximation we take  $r_f = r_s = 0$  as initial conditions for the  $h$ -current gating variables in the STI regime (after a spike has occurred).

In the remaining sections we study the dynamics of the SC using the reduced description described here.

## 3.3. Dynamics of the reduced SC model

In this section we study the mechanism of generation of STOs and MMOs in the SC model. These are generated from the dynamics of Eqs. (4)–(6).

The relative speed of  $r_f$  and  $r_s$  is given by the ratio of the right hand sides of Eqs. (5) and (6). The voltage deinactivation curves satisfy  $r_{f,\infty}(V) \sim r_{s,\infty}(V)$  (see Fig. 1(a)) and, in the range of values of  $V$  considered,  $\tau_{r_f}(V) \ll \tau_{r_s}(V)$  (see Fig. 1(c)). Initially,  $r_f \sim r_s (\sim 0)$ , due to the reset of  $I_h$ ; hence  $r_s$  is much slower than  $r_f$ , at least at the beginning

of the evolution process. For this reason we first study the three-dimensional reduced system (4)–(6) as a modulated two-dimensional system; i.e., we study two-dimensional systems of the form (4) and (5) slowly changing as  $r_s$  increases. We show that some important qualitative features of the dynamics of the reduced systems can be learned from this approach. However, the entire dynamic picture is not captured by it, as we show in Section 3.3.2.

### 3.3.1. Canard structures and a study of the reduced model with fixed values of $r_s$

The classic canard phenomenon is a sudden explosion of the small amplitude limit cycle created in a Hopf bifurcation (HB). This small amplitude limit cycle can be stable or unstable according to whether the HB point is supercritical or subcritical respectively. Here, we are concerned with the structure near an unstable limit cycle, and not the canard explosion itself. In most of this section, we discuss in as much generality as possible the structure that we use in analyzing our model. For easy applicability to (4)–(6), we use notation tailored to the model. For a more thorough introduction, we refer the reader to Eckhaus (1983), Dumortier and Roussarie (1996), Krupa and Szmolyan (2001).

The general equations have the form

$$\begin{cases} dV/dt = F(V, r_f; r_s), \\ dr_f/dt = \epsilon G(V, r_f), \end{cases} \quad (7)$$

where  $0 < \epsilon \ll 1$  and  $r_s$  is a fixed parameter. We assume that  $F = \mathcal{O}(1)$  and  $G = \mathcal{O}(1)$ , so that the two equations in (7) have well-separated time scales. We call  $r_f = N(V; r_s)$  the nullcline of the  $V$  equation (given by  $F(V, r_f, r_s) = 0$ ).

The dependence of  $F$  on  $r_s$  is assumed to be such that, as  $r_s$  increases,  $N(V; r_s)$  moves downward, possibly changing its shape. This is illustrated in Fig. 4(a) where  $\alpha > 0$  ( $\alpha$  represents an arbitrary value of  $r_s$ ). We call  $P(r_s)$  the fixed point of (7) corresponding to the leftmost intersection of the  $N(V; r_s)$  with nullcline of  $r_f$ . Note that with the shape of  $N(V; r_s)$  as in Fig. 4(a),  $P(r_s)$  moves to the right as  $r_s$  increases.

We call  $r_{s,M}$  the value of  $r_s$  corresponding to the nullclines intersecting at the maximum of  $N(V; r_s)$ . In Fig. 4(a),  $\alpha$  is very close to  $r_{s,M}$ . We further assume that Eq. (7) have a subcritical (unstable) Hopf bifurcation point  $P_H$  at some value  $r_{s,H} = r_{s,M} + \mathcal{O}(\epsilon)$  close to the maximum of  $N(V; r_s)$ . We also assume that for each  $r_s$  there is a point  $P_B(r_s)$  on the left branch of  $r_f = N(V; r_s)$  ( $r_s < r_{s,M}$ ), having the property that it separates those fixed points that are stable nodes from those that are stable spirals. In our model, without loss of generality, we are starting with  $r_s = 0$ . For  $r_s = 0$ , we assume  $P_B(0)$  is to the right of  $P(0)$  and for  $r_s = \alpha$ ,  $P_B(\alpha)$  is to the left of  $P(\alpha)$ ; our analysis

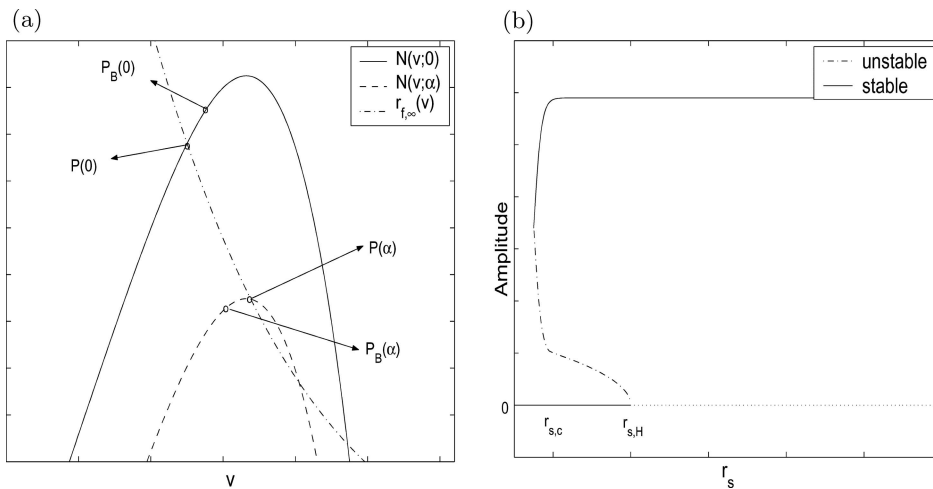


**Fig. 4** (a) Schematic representation of the nullclines  $N(V; r_s)$  and  $r_{f,\infty}(v)$  of system (7) for  $r_s = 0$  and  $r_s = \alpha > 0$ .  $P(r_s)$  represent fixed points,  $P_B(r_s)$  represent separatrix points dividing stable nodes and foci. As  $\alpha$  increases the nullcline  $N(V; r_s)$  moves down while the activation curve (nullcline)  $r_{f,\infty}(V)$  remains unchanged. (b) Schematic bifurca-

tion diagram for a subcritical Hopf bifurcation. An unstable limit cycle is born at the Hopf bifurcation point  $r_{s,H}$  out of a fixed point. This fixed point is stable to the left of  $r_{s,H}$ , and unstable (to the right of  $r_{s,H}$ ). The small amplitude limit cycle explodes in an exponentially small interval of values of  $r_s$  approximated by the point  $r_{s,c}$ .

uses that. Our assumptions reproduce the conditions of the real model for the parameters of interest. Note that, in the real model, the reset of  $I_h$  due to a spike (see Section 3.2.2) brings the trajectory to the initial condition  $r_s = 0$ .

There is an exponentially small (in  $\epsilon$ ) range of values of  $r_s$  (approximated by  $r_{s,c}(\epsilon) < r_{s,H}(\epsilon)$ ), inside which the canard explosion occurs (in the limit of  $\epsilon \rightarrow 0$ ). Figure 4(b) schematically shows the bifurcation diagram, including  $r_{s,H}$  and  $r_{s,c}$ , for a subcritical Hopf bifurcation. Note that the separation of scales in system (7) is necessary for the existence of the canard explosion.

Figure 5 illustrates the three behaviors of the system for different values of  $r_s$  in the presence of the above assumptions. In all three cases, we consider trajectories that first approach the  $V$ -nullcline and then stay close to it, moving slowly (Fig. 5(a)). That there are such trajectories is a consequence of the separation of time scales and the existence of an attracting invariant manifold close to the nullcline. The trajectory we are interested in (coming from the end of a spike) has this property.

For values of  $r_s \geq 0$  such that  $P(r_s)$  is to the left of  $P_B(r_s)$ , such trajectories approach the fixed point without oscillation; the attraction comes from the stability of the critical point  $P(0)$ . This is shown in (Fig. 5(a)).

For a value of  $r_s > 0$  such that  $P(r_s)$  is to the right of  $P_B(r_s)$  but is still stable, the critical point has trajectories spiraling inward. In this situation, as in the previous paragraph, the separation of time scales shapes the nature of the trajectories approaching the critical point. The trajectories now traverse across the maximum of  $r_f = N(V; r_s)$  (Fig. 5(b)). There is still an invariant manifold close to the  $V$ -nullcline,

but its attractiveness changes (in the limit as  $\epsilon$  goes to zero) to unstable to the right of the maximum. Nevertheless, the trajectory stays close to that invariant manifold in the “top” part of each spiral. This is what we refer to as the “canard structure”, and it is related to the mechanism by which small amplitude limit cycles blow up into large relaxation ones.

For some value of  $r_s$  still larger, but very close to the one corresponding to Fig. 5(b), the relevant trajectories do not spiral around the maxima of the  $V$ -nullcline (Fig. 5(c)). Instead, the trajectory moves across the maximum, close to the unstable small amplitude limit cycle created in the subcritical Hopf bifurcation (see Fig. 4), and leaves its neighborhood. Note that the canard phenomenon (explosion/implosion) occurs for values of  $r_s$  in between of those corresponding to Figs. 5(b) and (c). Note also that, in two dimensions, the requirement that trajectories do not cross each other prevents them from spiraling in, as long as an unstable small amplitude limit cycle surrounds the stable fixed point  $P(r_s)$ . For values of  $r_s > r_{s,H}$  the fixed point  $P(r_s)$  changes from stable to unstable and there is no longer an unstable limit cycle. In principle, trajectories starting close enough to  $P(r_s)$  spiral out and finally leave the  $N(v; r_s)$  knee neighborhood. However, the trajectories we are interested in have initial conditions far away from  $P(r_s)$ , and they approach the knee and leave its neighborhood without spiraling out.

In the above discussion, the separation of time scales was assumed, using  $\epsilon \ll 1$ . In (4) and (5), this separation of scales during the STI studied here is intrinsic to the system. It can be uncovered by defining  $\epsilon = C / (G_L T) = 0.025$  ( $T = 80$

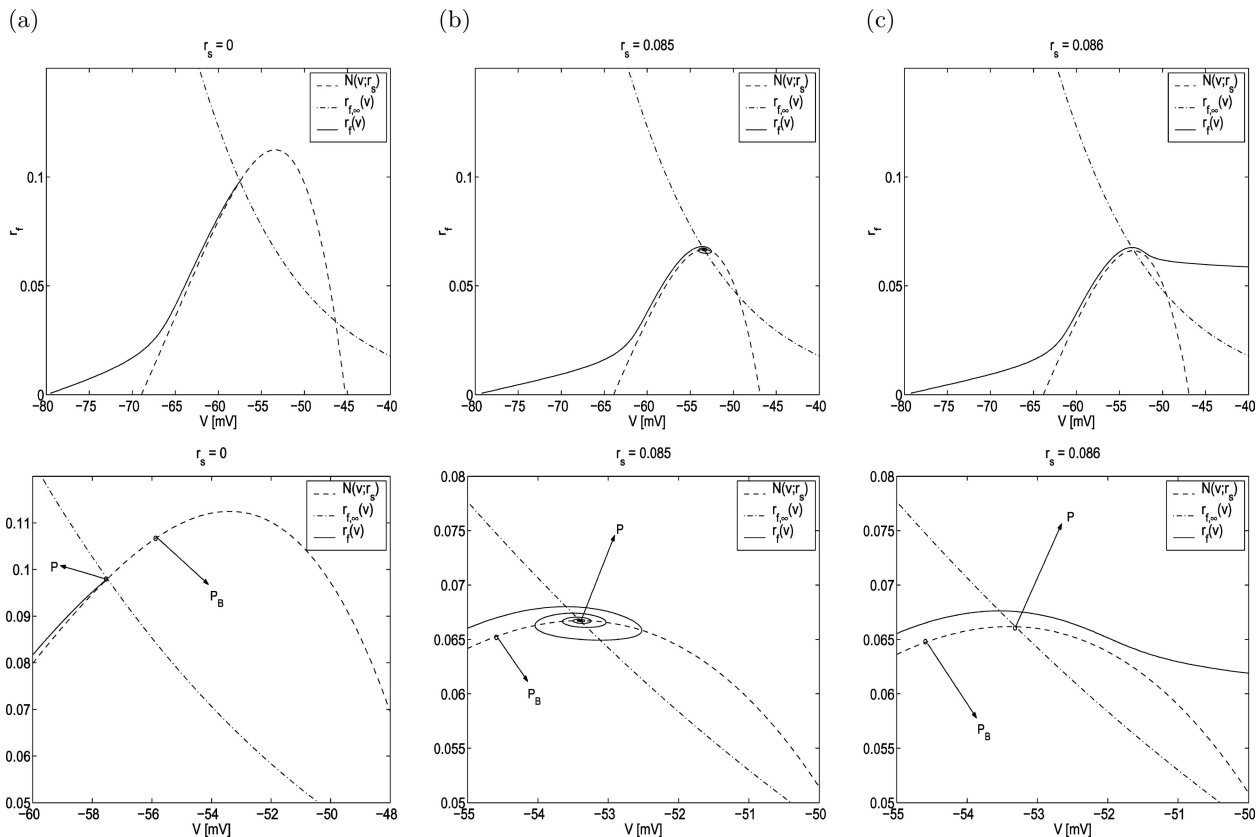


**Fig. 5** Phase diagram  $(V, r_f)$  for the reduced SC model for various values of  $r_s$  and  $G_h = 1.5$  and  $I_{app} = -2.5$ . The values of the other parameters used in the simulations are given in Section 2. Lower panels are magnifications of the upper ones.  $r_f(V)$  denotes a trajectory;  $r_{f,\infty}(V)$  and  $N(V; r_s)$  are nullclines. (a)  $r_s = 0$ : the trajectory converges

to a fixed point without spiraling. (b)  $r_s = 0.085$ : the trajectory spirals down to a fixed point. (c)  $r_s = 0.086$ : the trajectory moves around the knee of the nullcline  $N(V; r_s)$  and escapes the regime without spiraling.

msec is an appropriate time scale in the STO regime and  $|E_k|$  is an appropriate voltage scale). We pursue this elsewhere. From (4) and (5) the  $V$ -nullcline is now given by

$$\begin{aligned}
 N(V; r_s) &= \frac{I_{app} - G_p p_{\infty}(V)(V - E_{Na}) - G_h 0.35 r_s (V - E_h) - G_L (V - E_L)}{G_h 0.65 (V - E_h)} \\
 &= N(V; 0) - \frac{0.35}{0.65} r_s.
 \end{aligned}
 \tag{8}$$

Equations (4) and (5) satisfy the hypotheses above: As  $r_s$  is increased,  $N(V; r_s)$  moves downward (with a change of shape), and the leftmost critical point  $P(r_s)$  moves to the right. A standard stability analysis (not given here) shows that, for the lowest values of  $r_s$ ,  $P(r_s)$  is a stable node, as in Fig. 5(a). As  $r_s$  is increased,  $P(r_s)$  becomes a stable focus (Fig 5(b)). For a still larger value, the system undergoes a subcritical Hopf bifurcation in the neighborhood of  $N(v; r_s)$ . At still larger values of  $r_s$ , the trajectory leaves the neighborhood of the nullcline without oscillations. Indeed, Fig. 5(a–c) were drawn from Eqs. (4) and (5). For the full Eqs. (1)–(3),

leaving the neighborhood of the nullcline, with or without oscillations, corresponds to leaving the regime of the reduced equations and going into a regime in which the spiking components are important.

The time spent in each oscillation (decaying or expanding) is closely related to the time the trajectory of (4)–(6) spends moving along the slow manifold  $N(V; r_s)$ . Thus, the canard structure, which forces the trajectory to stay close to the invariant manifold at the “top” portion of the oscillations, imposes a time scale for the STO.

### 3.3.2. A three-dimensional approach: Generation of subthreshold oscillations

Here we study system (4)–(6). As explained at the beginning of Section 3.3  $r_s$  evolves slower than  $r_f$  at the beginning of the STO regime. From Fig. 3 (the second panel is a blow up of the first one) it is apparent that  $r_f$  and  $r_s$  do not evolve in different time scales; our calculations show that  $r_s$  is at most four times slower than  $r_f$  and is approximately the same as

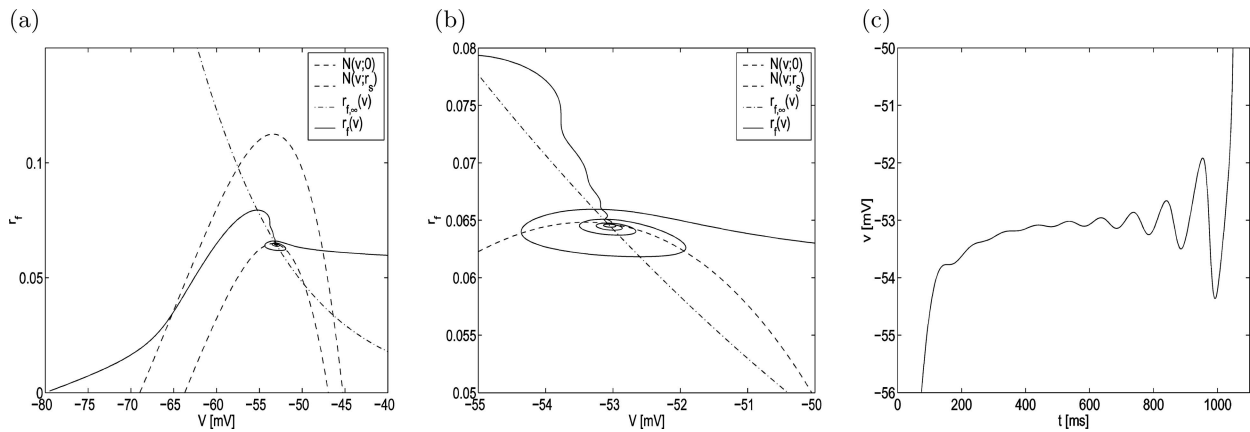


**Fig. 6** Dynamics of the reduced SC model for  $G_h = 1.5$  and  $I_{app} = -2.5$ . The values of the other parameter used in the simulations are given in Section 2. (a) Trajectory for  $r_f$  and  $V$  when  $r_s$  evolves continuously.  $N(V; 0)$  and  $N(V; r_s)$  are the upper and lower  $V$ -nullclines respectively. The latter was calculated for an approxima-

tion of the highest value of  $r_s$ . (b) Magnification of panel (a). Note that when the trajectory escapes the regime (corresponding to the SC firing an action potential), it does so at the same voltage at which the previous STO reached its maximum. (c) voltage trace showing STOs.

$r_f$  near the end of the STO regime. However, at least in part of the STI, the separation of scales is still large enough to allow the heuristic study of the dynamics of Eqs. (4)–(6) by looking at continuously evolving phase planes (of the type discussed in Section 3.3.1) for Eqs. (4) and (5), each one corresponding to a specific value of the evolving variable  $r_s$ . Similar problems (Drover et al., 2004) have been shown to be different from the classical slow passage through the Hopf bifurcation (e.g. Neishtadt, 1987, 1988; Baer et al., 1989).

Our results are shown in Figs. 6 and 7. (The schematic Fig. 4(a) is helpful in this explanation too.) As  $r_s$  evolves, the  $V$ -nullcline  $N(V; r_s)$  continuously moves down (see Eq. (8)), generating a two-dimensional slow manifold. In Fig. 6(a) we show two of these nullclines, corresponding to  $r_s = 0$  (top nullcline) and to a value  $r_s > 0$  (bottom nullcline). Figure. 6(b) and 7 are (two- and three-dimensional) blow-ups of Fig. 6(a). In Fig. 7 we can see the two-dimensional slow manifold  $N(V; r_s)$  and the nullsurface  $r_{f,\infty}(V)$  (which is independent of  $r_s$ ).  $P(r_s)$ , which is also continuously evolving, generates a segment of a curve contained in the graph of  $r_{f,\infty}(V)$ . (In Fig. 4(b) this curve contains the points  $P(0)$  and  $P(\alpha)$ ). There are two other relevant curves parametrized by  $r_s$ , the fold curve  $L$  joining the maxima of  $N(v; r_s)$  and the separatrix curve  $L_B$  joining the points  $P_B(r_s)$  (not shown in the Figs.). Since initially  $r_s = 0$  and  $P(0)$  is a node (placed to the left of  $P_B(0)$  as shown in the schematic Fig. 4(b)), as  $r_s$  increases,  $r_{f,\infty}(V)$  intersects both  $L$  and  $L_B$ . Note that by intersecting the nullsurface  $N(V; r_s)$  with planes  $r_s = k$  ( $k > 0$  constant) one recovers the nullclines  $N(V; k)$  corresponding to two-dimensional systems, as described in Section 3.3.1. Values of  $P(r_s)$  to the right of  $L_B$  and close enough to  $L_B$  correspond to stable foci in  $N(V; k)$ , and for some values of  $r_s$  such that  $P(r_s)$  is to the right of  $L$ ,  $P(r_s)$  are to the left of the HB point.

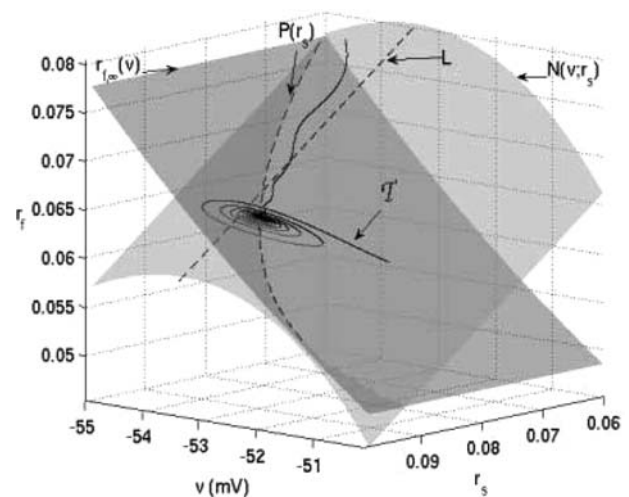


**Fig. 7** Dynamics of the reduced SC model for  $G_h = 1.5$  and  $I_{app} = -2.5$ . The values of the other parameter used in the simulations are given in Section 2. The  $V$ - and  $r_f$ - nullsurfaces ( $N(V; r_s)$  and  $r_{f,\infty}(V)$ ) intersect at  $P(r_s)$ . The line  $L$  joins the local maxima of  $N(V; r_s)$  corresponding to fixed values of  $r_s$ . The trajectory  $T$  oscillates and escapes the STO regime.

We use both two- and three-dimensional approaches in our explanation.

Due to the separation of time scales (between the fast variable  $V$  and the slow variables  $r_f$  and  $r_s$ ), the trajectory  $T$  starting at  $(V_0, r_{f,0}) = (-80, 0)$  stays close to the manifold  $N(V; r_s)$  and moves towards  $P(r_s)$ . The 2D points  $P(r_s)$  are not fixed points (in the three-dimensional view); they are target points towards which the trajectory moves. In Fig. 6(a) we see the trajectory moving up and to the right until it intersects the “curve of fixed points” ( $r_{f,\infty}(V)$ ). Note that the speeds of  $r_s$  and  $r_f$  in Fig. 3 are not constant, but decrease and become of the same order of

magnitude as these variables approach the STO regime. When  $\mathcal{T}$  gets close enough to the knee of  $N(V; r_s)$  and  $r_s$  is such that  $P(r_s)$  corresponds to a focus in a two-dimensional view,  $\mathcal{T}$  oscillates, staying close to the slow manifold  $N(V; r_s)$ . The amplitude of the oscillations decreases as  $P(r_s)$  approaches the curve  $L$ . In Fig. 6(a) these oscillations are the ones with decreasing amplitude in between the two nullclines. In the two-dimensional view, this corresponds to “spiraling down” to a fixed point. As this happens, the speed of  $r_s$  decreases,  $r_s' \sim r_f'$ , and the two-dimensional approach breaks down. Indeed, one cannot invoke it to explain the oscillations with increasing amplitude around the bottom nullcline in Figs. 6 and 7. Heuristically, past the HB point, the restriction imposed on 2D systems by the unstable limit cycle is not relevant (due to the extra dimension in the 3D system), and there is no longer an impediment for  $\mathcal{T}$  to spiraling outward in the locally relevant 2D analogue. Thus, as  $r_s$  increases further,  $P(r_s)$  moves to the right of the HB point and the trajectory escapes this regime to the spiking one, where  $I_{Na}$  and  $I_K$  get activated. However, the 2D picture is not an accurate one in the vicinity of the knee. In this region the time scale differences disappear and  $r_s$  is involved in the oscillations with increasing amplitude along with the remaining variables. In this region  $r_s$  is no longer a modulatory variable and we do not have a 2D structure in which  $N(V; r_s)$  moves monotonically with  $r_s$ .

The facts just described, together with the shape of the trajectory in Fig. 6(b) and some preliminary calculations (not presented here), suggest we are in the presence of a canard phenomenon in  $R^3$  (Szmolyan and Wechselberger, 2001; Wechselberger, 2005); i.e., trajectories are trapped in a transient rotational “funnel” for a significant amount of time. Since this behavior is transient, eventually the trajectory exits the funnel and typically jumps along a fast direction either to the left (producing one last rotation) or to the right (Wechselberger, 2005; Brons et al., 2005). In Fig. 6(b) we can see this last rotation (with an amplitude significantly larger than the previous ones) before the trajectory escapes the STO regime.

A rigorous explanation of the STO mechanism in terms of the canard phenomenon in  $R^3$  is beyond the scope of this manuscript, mainly because of the complexity of the tools needed (Wechselberger, 2005; Drover et al., 2004).

The number and amplitude of the STOs is affected by the speed of  $r_s$ : The slower  $r_s$ , the more STOs are developed, since  $\mathcal{T}$  spends more time near the knee. On the other hand, if  $r_s$  evolves fast enough,  $\mathcal{T}$  does not spend enough time near the knee for even one STO to be generated. In the reduced SC model, the speed of  $r_s$  is not uniform but decreases with time (see Fig. 3). To the first approximation, it is faster for values of  $r_s < r_{s,M}$  ( $P(r_s)$  to the left of the curve  $L$ ) than for values of  $r_s > r_{s,M}$ . Thus, there may be fewer STOs

with decreasing amplitude. As a consequence the STOs with decreasing amplitude are hard to see.

### 3.3.3. A stellate cell nonlinear artificially spiking (NAS) model

The fact that  $I_{Na}$  and  $I_K$  are inactive during the STO regime suggests that if one is not interested in the spike details but only in the generation of a spike, the dynamics of the SC can be approximately described by a nonlinear artificially spiking (NAS) model consisting of Eqs. (4)–(6) supplemented with an artificial spike. The onset of spikes is described by the dynamics of Eqs. (4)–(6). In our simulations we give an appropriate threshold value,  $V_{th} = -10$  mV to indicate that the trajectory is moving along a fast direction towards the spiking regime. More negative values may be good as well. We give also a reset value,  $V_{rst} = -80$  mV, which is a good approximation to the reset value in the full SC model. According to Section 3.2.2, a good approximation to the reset values of the  $h$ -current gating variables are  $r_f = r_s = 0$ .

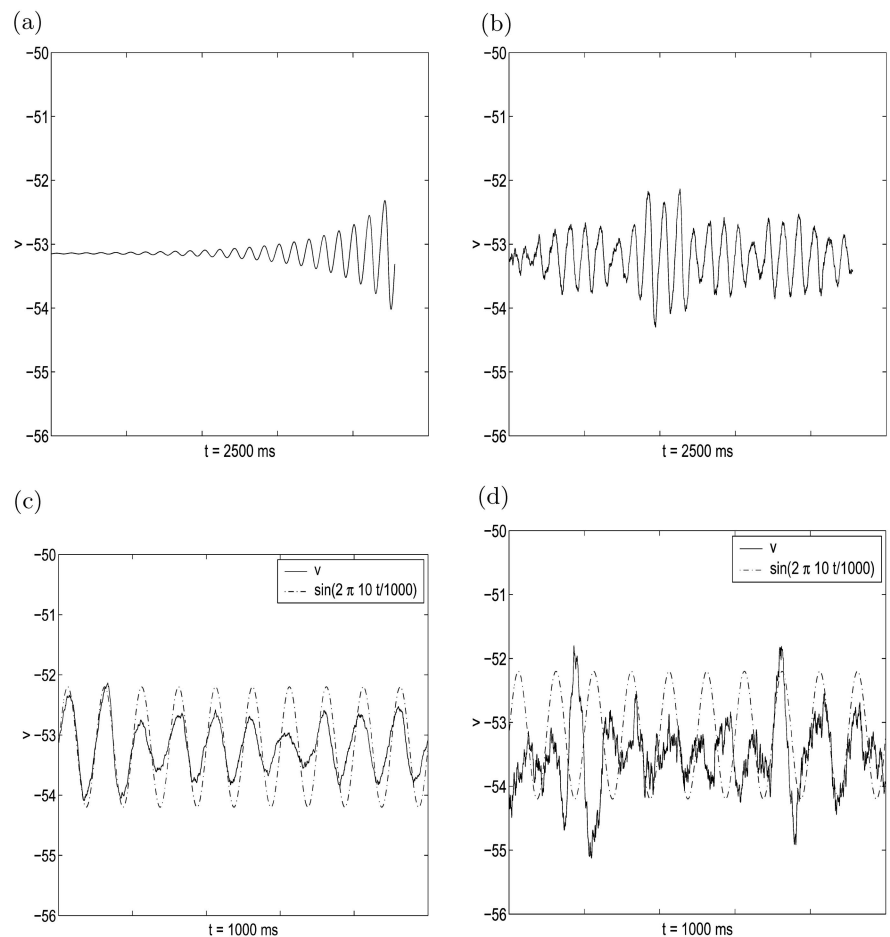
In the full SC model there is a brief intermediate regime in between the spiking regime and the STO regime studied here. This regime corresponds to the recovery of the voltage after a spike. It is different from the STO regime studied here in that  $I_K$  is an active current and its gating variable  $n$  evolves on a time scale faster than both  $r_f$  and  $r_s$ ; i.e.  $n$  is a dynamic variables interacting with  $v$ . In this regime, both  $r_f$  and  $r_s$  evolve slowly from their reset values for a short amount of time, so these reset values are still a good approximation.

NAS type models include the generalized integrate- and resonate-and fire (GIF and GRF) models (Izhikevich, 2001; Richardson et al., 2003). In the generalized integrate-and-fire models used by Richardson et al. (2003) to study resonance effects, there is either a two-component  $I_h$  or a  $I_{Nap}$  and  $I_{Ks}$  (slow  $K^+$  current). To our knowledge no NAS model has been proposed having both  $I_h$  and  $I_{Nap}$ . Our NAS model describes the STI with asymptotic accuracy and is a good approximation of the full SC model (1)–(3).

### 3.4. Robust subthreshold oscillations in a noisy NAS SC model

In Section 3.3 we explained the mechanism of generation of STOs for the reduced SC model, which is deterministic. One of the features of deterministic SC models is that, for physiologically plausible parameters (and consequent speeds of  $r_s$ ), STOs and mixed mode patterns are unlike those seen in experiments. If the STOs generated by the SC model do not decay to resting potential, they increase their amplitude until an action potential is fired (see Fig. 6(c)). In the latter case, the temporal patterns are regular. In Fig. 8(a) we show the voltage trace for a value of  $I_{app}$  just above this corresponding to the

**Fig. 8** STOs for noiseless and noisy systems for  $G_h = 1.5$ . The values of the parameter used in the simulations are given in Section 2. (a)  $D = 0$  and  $I_{app} = -2.55$ . In the absence of noise the amplitude of the STOs increase uniformly with time and eventually the SC fires an action potential. In the figure we show the STOs occurring in the basic time interval (up until the first spike). For  $I_{app} = -2.58$  and  $D = 0$  the SC is silent (data not shown). (b)  $D = 10^{-6}$  and  $I_{app} = -2.58$ . STOs are produced in the presence of noise, but the amplitude does not increase uniformly with time. For comparison we show the STOs not exceeding the basic time interval (for the same amount of time as in Fig. (a)). (c)  $D = 10^{-6}$  and  $I_{app} = -2.58$ . Comparison of the STOs produced in the noiseless case with a sinusoidal function (10 Hz). (d)  $D = 2.5^{-5}$  and  $I_{app} = -2.7$ . Comparison of the STOs produced in the noiseless case with a sinusoidal function (10 Hz). The value of  $D$  is larger as compared to the one in (c) and the STOs are more influenced by noise.



cell decaying to resting potential. We ended the simulation at a time right before the first spike occurred. (We will call this maximal time interval  $T_{STO,max}$ .) In experiments, however, when the membrane potential is depolarized from resting potential to a value below spiking threshold, STOs at a theta frequency are generated with no apparent amplitude pattern. See Section 1 for references.

Various modeling studies have introduced channel noise in order to obtain robust STOs. White et al. (1998) showed that the number of persistent  $Na^+$  channels underlying STOs is relatively small, and argued that the stochastic behavior of these channels may contribute crucially to the cellular-level responses. In their study they used a biophysical stochastic-deterministic model having  $I_{Nap}$  and  $I_{Ks}$  in addition to the standard HH currents. The  $I_{Nap}$  they used was represented by a population of stochastic ion channels. Using this model they found regimes in which STOs and spikes coexist. More recently, Fransén et al. (2004) used a noisy model having  $I_{Nap}$  and a two-component  $I_h$ . They concluded that, although noise is not required for the SC to display STOs, its presence increases their robustness.

Here we first show that, consistent with the findings mentioned in the previous paragraph, our SC model is able to produce robust STOs. Secondly, we discuss the conditions under which STOs are more regularly seen. Finally, by studying the effect of deterministic perturbations to fixed points, we show how the effects of noise can be explained using the canard structure framework discussed in previous sections.

### 3.4.1. Noise generated STOs: Simulations

Following White et al. (1998) we introduce channel white noise in  $I_{Nap}$ . We do that in a way that is simple enough to give an explanation of the mechanism of generation of robust STOs due to noise effects. (We do not claim that our approach is the most appropriate biophysically plausible one.) More specifically, we add a stochastic term  $\sqrt{2D} \eta(t)$  to the dynamic equation for  $p$ . This term is delta correlated with zero mean; i.e.,  $\langle \eta(t), \eta(t') \rangle = \delta(t - t')$ .  $D > 0$  is the standard deviation. Since  $p$  is slaved to  $v$ , we substitute  $p_\infty(v) + \tau_p(v) \sqrt{2D} \eta(t)$  for  $p_\infty(v)$  in Eq. (4).

In order to get results qualitatively similar to the findings of other authors (e.g., see Fransén et al. (2004)) the value

of the tonic drive needs to be set to  $I_{\text{app}} = I_{\text{app}}^0 = -2.58$ , so that in the absence of noise the SC is silent (the trajectory evolves towards a stable fixed point) but, for a slightly higher value of  $I_{\text{app}}$ , the cell displays MMOs (STOs and spikes). For example, the voltage traces for a noiseless system ( $D = 0$ ) shown in Fig. 8(a) correspond to  $I_{\text{app}} = -2.55 > I_{\text{app}}^0$ . The ones shown in Fig. 8(b) correspond to a noisy system ( $D = D_M = 10^{-6}$ ) and  $I_{\text{app}} = I_{\text{app}}^0$ . In the noisy system, the STOs have no monotonically increasing amplitude. These persistent STOs are possible due to stochastic fluctuations, since  $I_{\text{app}}^0$  corresponds to a deterministic silent cell. The value  $D_M$  is approximately the largest value of  $D$  for which the SC displays only STOs in the time interval  $T_{\text{STO,max}}$ .

In Fig. 8(c) we compare the voltage trace of the SC presented in Fig. 8(b) with a 10 Hz sinusoidal function, to show that the noisy SC oscillates at approximately this frequency. The power spectrum of the STOs in Fig. 8(b) and 8(c) have a well defined peak at 10 Hz (data not shown).

If one chooses a value of  $I_{\text{app}} < I_{\text{app}}^0$  (making the cell silent and further away from the STO regime), one can still get STOs with a theta frequency component, provided the value of  $D$  is considerably increased (by a factor of 25). As an illustration, Fig. 8(d) shows the voltage traces for  $I_{\text{app}} = -2.7$  and  $D = 2.5 \times 10^{-5}$ . There the agreement with a 10 Hz sinusoidal function is not as good as in the previous case discussed and the voltage trace appears noisier than in Fig. 8(c) (where  $I_{\text{app}} = I_{\text{app}}^0$ ).

Our simulations all show that, as  $D$  decreases, the frequency preference is kept, but the amplitude of the STOs decreases (data not shown). Qualitatively similar results have been obtained for other similar parameters regimes. In all parameter regimes considered, robust STOs similar to the ones shown in Fig. 8(b) were found, provided  $I_{\text{app}}$  was such that the SC is silent but close to the STO regime.

### 3.4.2. Noise generated STOs: The role of the canard structure

A heuristic explanation of the effect of noise can be achieved by using the canard structure framework described in former sections. As before, we view the dynamics of the three-dimensional system as a two-dimensional system with  $r_s$  moving the  $V$ -nullcline  $N(V; r_s)$  and generating a two-dimensional slow manifold. In Fig. 9 we show phase space diagrams analogous to those in Fig. 6 corresponding (from 9(a) to 9(c)) to the STO-noiseless cell ( $I_{\text{app}} = -2.55$  and  $D = 0$ ), silent-noiseless cell ( $I_{\text{app}} = -2.58$  and  $D = 0$ ) and STO-noisy cell ( $I_{\text{app}} = -2.58$  and  $D = 10^{-6}$ ). Note that Figs. 9(a) and (c) are the phase diagrams of Figs. 8(a) and (b) respectively. The bottom panels represent blow-ups of the upper ones.

In all three cases the trajectory moves fast towards the slow manifold  $N(V; r_s)$  and approaches the region of “knees”. In

the STO-noiseless case (Fig. 9(a)), as in Fig. 6, the trajectory rotates and escapes the STO regime. In Fig. 9(b) (silent-noiseless case), the trajectory reaches a fixed point and stays silent (the value of  $I_{\text{app}}$  is lower than the one in Fig. 9(a)). In Fig. 9(c) the values of the parameters are as in 9(b) but the system is noisy ( $D = D_M = 10^{-6}$ ), so the trajectory oscillates around the knee. (As in Fig. 8 spikes are not produced in the maximal time interval  $T_{\text{STO,max}}$ .) These oscillations (and their amplitude) are the result of the trajectory being attracted to the unstable manifold of the  $V$ -nullsurface for a certain (and large enough) interval of time in successive cycles instead of decaying rapidly to a fixed point or escaping the STO regime.

To investigate further the role of the canard structure in the generation of STOs via noise, we study the evolution of (deterministic) perturbations to the silent cell steady state  $P_{ss} = (V_{ss}, r_{f,ss}, r_{s,ss})$  for the two set of parameters ( $I_{\text{app}} = I_{\text{app},0} = -2.58$  and  $I_{\text{app}} = -2.70$ ) corresponding to Figs. 8(c) (whose phase diagram is given in Fig. 9(c)) and 8(d) respectively. Increasing values of  $I_{\text{app}}$  place the system closer to the canard regime; i.e.,  $P_{ss}$  is closer to the bifurcation where it loses stability for  $I_{\text{app}} = -2.58$  (Fig. 8(c)) than for  $I_{\text{app}} = -2.7$  (Fig. 8(d)). We will show that in both cases there is a neighborhood (in 3D space) of the fixed point  $P_{ss}$  such that trajectories starting inside this neighborhood spiral down towards  $P_{ss}$  following the  $V$ -nullsurface unstable manifold for a significant interval of time before crossing to the stable one. This spiraling down is slower the higher the value of  $I_{\text{app}}$ , and it is particularly slow for  $I_{\text{app}} = -2.58$ , so the amplitude of the oscillations resulting from perturbations is maintained for many cycles. We start by looking at this regime (Fig. 10(a)) and we contrast our findings with the  $I_{\text{app}} = -2.70$ -regime (Fig. 10(b)) where the amplitude of the oscillations decreases much faster and a larger value of  $D$  is required to get a theta frequency component in the voltage traces.

In Fig. 10,  $P_{ss}$  is the intersection of the curves  $N(V; r_{s,ss})$  and  $r_{f,\infty}(V)$ . All panels correspond to perturbations to  $P_{ss}$  such that  $V$ -component of the new initial conditions  $(V_0, r_{f,0}, r_{s,0})$  is to the right of  $V_{ss}$  ( $V_0 > V_{ss}$ ). The left and right panels correspond to very close initial conditions leading to trajectories spiraling down towards  $P_{ss}$  or escaping the STO regime (the trajectories cross the plane  $V = -50$  and continues to grow).

For  $I_{\text{app}} = -2.58$  (Fig. 10(a)),  $P_{ss}$  is such that  $V_{ss} = -53.213757$ ,  $r_{f,ss} = 0.065552$  and  $r_{s,ss} = 0.091690$  and the initial conditions  $(V_0, r_{f,0}, r_{s,0})$  have been set equal to  $(-52.451, r_{f,ss}, r_{s,ss})$  (left panel) and  $(-52.450, r_{f,ss}, r_{s,ss})$  (right panel). For other perturbations to the right of  $V_{ss}$  such that  $V_0 < -52.451$  or  $V_0 > -52.450$  trajectories spiral inward or outward respectively. These trajectories do not evolve in a plane; the  $r_s$  component oscillates with an amplitude whose order of magnitude is that of  $r_f$  (not shown). The

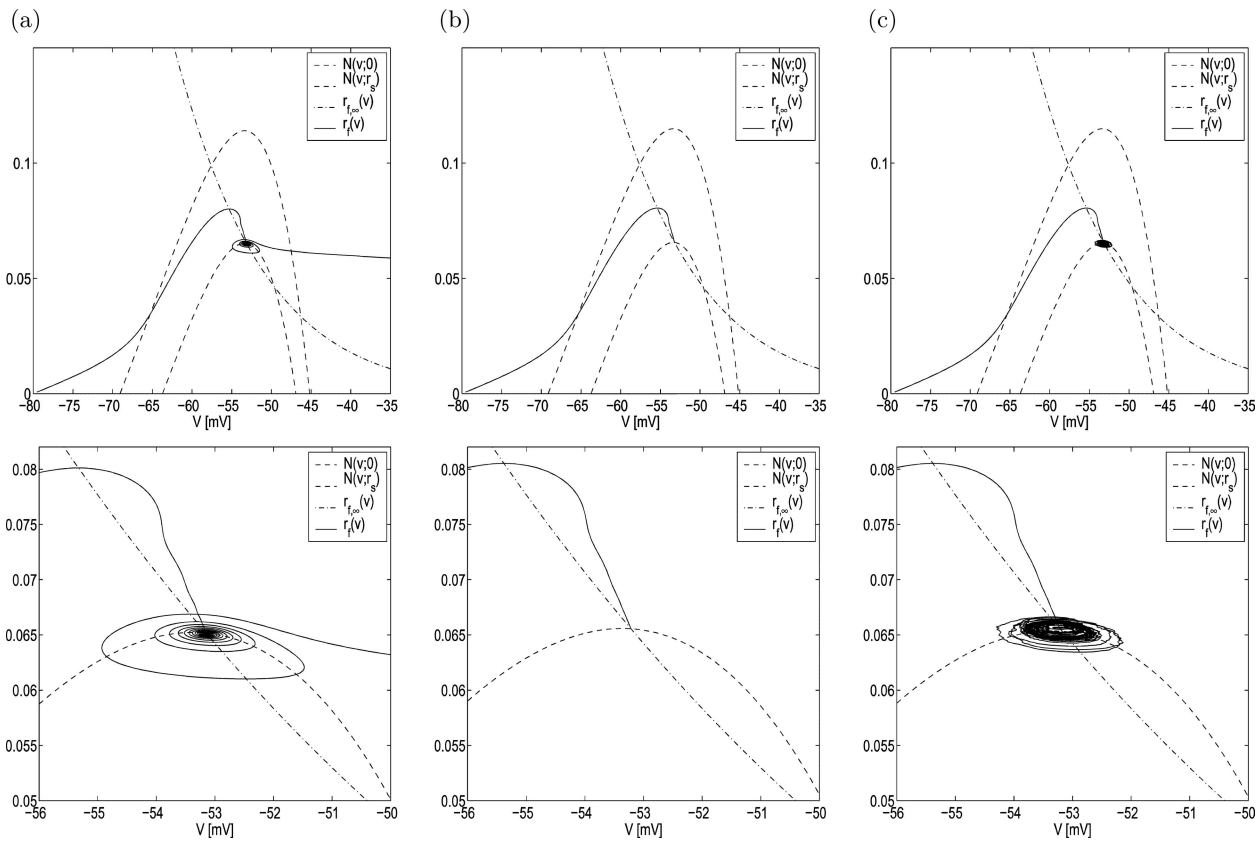


**Fig. 9** Dynamics of the reduced SC in the noiseless and noisy cases. Trajectories ( $r_f(V)$ ) when  $r_s$  varies continuously.  $N(V; 0)$  and  $N(V; r_s)$  are the upper and lower  $V$ -nullclines respectively. The latter was calculated for an approximation of the highest value of  $r_s$ . The bottom

panels are magnifications of the top ones. (a)  $D = 0$  and  $I_{app} = -2.55$  (noiseless STOs). (b)  $D = 0$  and  $I_{app} = -2.58$  (noiseless silent cell). (c)  $D = 10^{-6}$  and  $I_{app} = -2.58$  (noisy STOs).

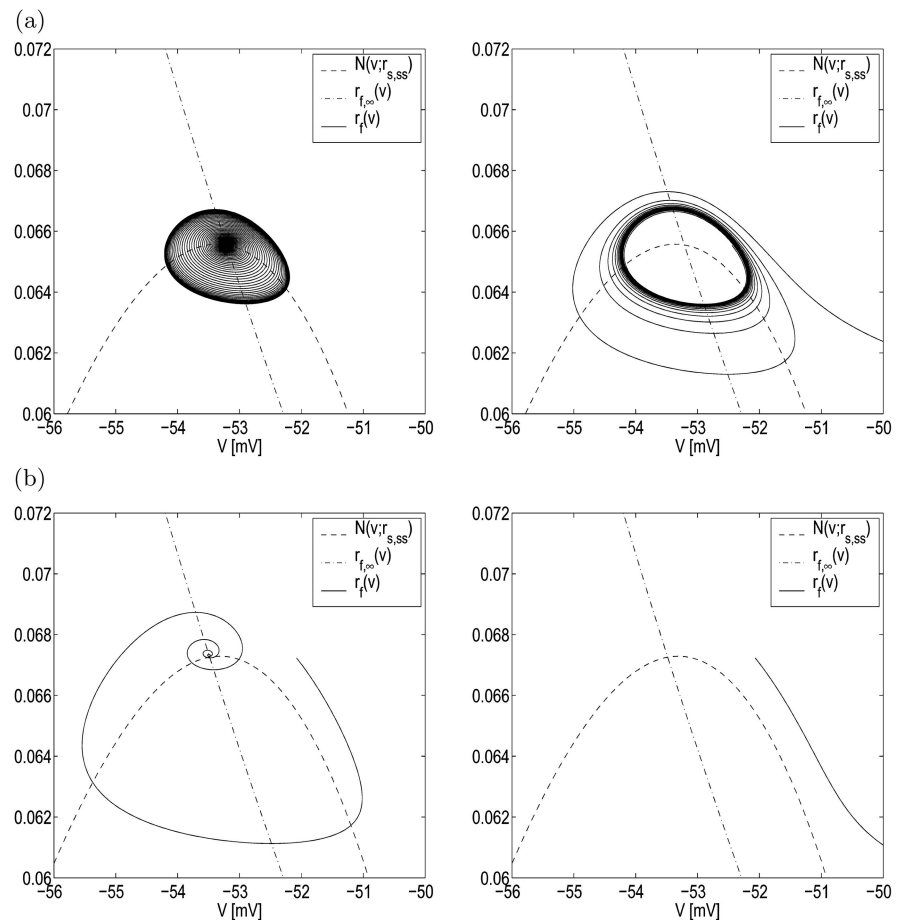
amplitude of the spiraling inward trajectories decreases very slowly; i.e., these trajectories are tightly packed. So consecutive cycles have almost the same amplitude and the frequency of the oscillations, determined by the canard structure, is almost constant. Another feature of trajectories spiraling inward (Fig. 10(a), left panel) is that amplitude perturbations of the same magnitude in different directions have differentiated effects. For example, let us consider perturbations up and down from  $P_{ss}$  (in the  $r_f$  direction). We can see in Fig. 10(a), (left panel) that the magnitude of the perturbation up needed to bring the trajectory to the boundary of the basis of attraction of  $P_{ss}$  is lower than the magnitude of the perturbation down needed to bring the trajectory to the same situation. We obtained qualitatively similar results for perturbations including changes in the  $r_s$  direction (not shown).

The effects of noise can be heuristically explained as perturbations (stochastic rather than deterministic) to the underlying dynamic structure (given by the nullsurfaces) of the type described in the previous paragraph. In the mean, this structure is as in Fig. 9(b); i.e., as in the deterministic version where the SC is silent. As a consequence of the stochastic

perturbations,  $P_{ss}$  will no longer be fixed, and the nearby dynamics determines how trajectories will move. If the trajectory is initially at  $P_{ss}$  and  $D$  is small enough, the trajectory will be left in the basin of attraction of  $P_{ss}(t)$  and it will evolve (approximately) according to the dynamics described in Fig. 10(a), which is deterministic; i.e., it will oscillate with a slowly changing amplitude. This amplitude will be larger the further away from  $P_{ss}(t)$  the trajectory is left; and, for the same magnitude of the noisy perturbation, it will be larger if the trajectory is left above the  $V$ -nullsurface than below it. The continuing effect of noise maintains the trajectory moving around the knee with almost uniform frequency and amplitude. As in the deterministic case, both are dictated by the canard structure; i.e., by the time the trajectory spends moving along the  $V$ -nullsurface unstable manifold.

Let us look now at the regime where  $I_{app} = -2.70$  (Fig. 10(b)) corresponding to Fig. 8(d) (higher noise as compared to the case discussed previously).  $P_{ss}$  is such that  $V_{ss} = -53.482613$ ,  $r_{f,ss} = 0.067261$  and  $r_{s,ss} = 0.095361$ ; and it is further away from the knee than in the regime discussed in the previous paragraphs. The initial conditions ( $V_0, r_{f,0}, r_{s,0}$ ) have been set equal to  $(-52.09, r_{f,ss}, r_{s,ss})$

**Fig. 10** Phase diagrams for deterministic perturbations to the stable fixed points  $P_{ss} = (V_{ss}, r_{f,ss}, r_{s,ss})$ . In all cases  $r_{f,init} = r_{f,ss}$  and  $r_{s,init} = r_{s,ss}$ . (a)  $I_{app} = -2.58$ ,  $P_{ss} = (-53.213757, 0.065552, 0.091690)$ ,  $V_{init} = -52.451$  (left) and  $V_{init} = -52.45$  (right). The trajectory displays STOs with slowly changing amplitude (left) or escapes the STO regime after performing STOs (right). (b)  $I_{app} = -2.70$ ,  $P_{ss} = (-53.482613, 0.067261, 0.095361)$ ,  $V_{init} = -52.09$  (left) and  $V_{init} = -52.08$  (right). The trajectory displays STOs with rapidly changing amplitude (left) or escapes the STO regime without performing STOs (right).



(left panel) and  $(-52.08, r_{f,ss}, r_{s,ss})$  (right panel). In both cases  $V_0$  is in the vicinity of the  $V$ -nullsurface unstable manifold, but in the latter case the trajectory is not close enough to that manifold, so it escapes the STO regime (it crosses the plane  $V = -50$  and  $V$  continues to grow). Fig. 10(b) (left panel) shows that, in contrast to Fig. 10(a), the oscillations are less packed and their amplitude is much less uniform (decays faster) compared to the ones in Fig. 10(a). Qualitatively similar results were obtained for perturbations including changes in the  $r_s$  direction (not shown).

In contrast to the regime where  $I_{app} = -2.58$ , here noisy perturbations in different directions have different dynamic effects. We show this schematically in Fig. 11. The square around the fixed point is a representation of the region where the trajectory is assumed to be left after any perturbation if it was previously at the fixed point. We call  $\bar{R}_j$  ( $j = I, II, III, IV$ ) the intersection between the square and each of the regions  $R_j$ , not including the fixed point. Each pulse moves the fixed point and leaves the trajectory in one of the regions  $\bar{R}_j$ . Trajectories in  $\bar{R}_I$ ,  $\bar{R}_{III}$  or  $\bar{R}_{IV}$  converge to the stable fixed point performing very small amplitude oscillations. Region  $\bar{R}_{II}$  is a distinguished case. Trajectories starting there are unable to come back to the stable fixed point without going around the knee and so performing a

STO. Unless continuing noise is strong enough to push a trajectory in  $R_{II}$ , and close enough to  $P_{ss}$ , back to any of the other regions, this trajectory stays in  $R_{II}$  and a STO is forced. Since, after the first STO, the amplitude of trajectories in  $R_{II}$  rapidly decreases, the noise magnitude needed to maintain STOs with an amplitude similar to that in the  $I_{app} = -2.58$  case, has to be stronger than in the  $I_{app} = -2.58$  regime, and the voltage traces become noisier (see Fig. 8(d)). However, the frequency of these STOs is still dictated by the canard structure.

#### 4. Discussion

Subthreshold membrane potential oscillations have been observed at various locations in the brain (Llinás and Yarom, 1981, 1986; Alonso and Llinás, 1989; Hutcheon et al., 1996; Dickson et al., 2000b; Erchova et al., 2004). In the last years, the study of STOs in the MEC has received special attention from both the experimental and theoretical point of view (see references in Section 1). The results presented in this manuscript contribute to the understanding of the biophysical mechanism of this phenomenon. While previous theoretical studies were based on simulations, we focus here on the

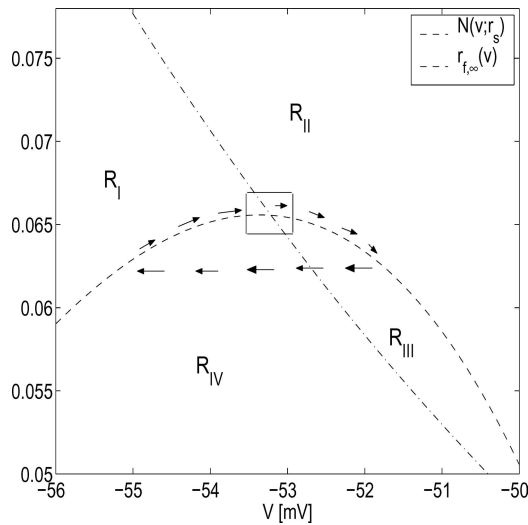


**Fig. 11** Schematic diagram of the nullclines  $N(V; r_s)$  and  $r_{f,∞}(V)$ . The square encloses possible perturbations from the fixed point. The arrows show the direction of motion of trajectories.

dynamic framework (canard structure) underlying the numerical results.

The structure we have uncovered is intrinsically three-dimensional. We note that STOs and MMOs can be produced by other mathematical mechanisms in two-dimensional models with noise, both linear and nonlinear, (e.g., Izhikevich, 2001; Makarov et al., 2001). We are interested here in the particular dynamical mechanism uncovered from a detailed biophysical model of the SCs, a mechanism which is wholly different from that of the linear or nonlinear two-dimensional models with noise. The two-dimensional (Makarov et al. (2001) model, while reproducing some aspects of biophysical models, is a description of inferior olive STOs (and MMOs) and does not contain the specific biophysical details thought to be important for MEC SCs.

One may ask whether the two-dimensional models with noise can reproduce the phenomenon observed in SCs in a way that is faithful to known experimental facts. Our model, built on known detailed biophysics, makes the prediction that the slow component of the  $h$ -current (third dimension) plays a critical role in the generation of STOs and MMOs. This prediction can differentiate between the dynamical mechanism presented here and two-dimensional models, which do not have any extra slow variable. Further theoretical and experimental work may help to illuminate the circumstances under which the different mechanisms operate.

It was already known that the interaction between  $I_{Nap}$  and  $I_h$  is enough to account for the generation of STOs in layer II of the MEC. However, the specific role of each one of these currents, in particular the fast and slow components of  $I_h$  and the dynamics of their interaction, was not yet understood. To answer these questions we looked at a bio-

physical single-cell model that has been used in the past to study synchronization properties of SCs. We demonstrated that this seven-dimensional model can be approximated by a reduced three-dimensional model in the STI, where STOs are observed. This approximation is based on the fact that the spiking generation currents ( $I_{Na}$  and  $I_K$ ) are not active in the STI regime (this is not always true for spiking models, as explained in Section 3.2.1). Furthermore, there is a clear separation of scales between the voltage ( $V$ ) and the two  $I_h$  gating variables ( $r_f$  and  $r_s$ ). This, together with the arrangement of the nullsurfaces in the three-dimensional phase space, creates what we call the canard structure. This structure serves as the basic framework to understand the dynamic aspects of the generation of STOs and MMOs (coexistence of STOs and spikes). In the absence of  $r_s$  as a dynamic variable, the  $V$  and  $r_f$  nullclines intersect at a fixed point that is a stable node, stable focus or unstable focus. Thus, in the noiseless case, trajectories can either converge to a fixed point (in an oscillatory fashion or not) or spike. No MMOs are possible. The role of  $r_s$  is, roughly speaking, to serve as a bridge between both dynamic behaviors, allowing for coexistence of STOs and spikes. More specifically, after the reset of  $I_h$  (due to a spike),  $r_s$  first evolves much slower than  $r_f$  and  $V$ . Even though  $r_f$  and  $r_s$  differ by less than an order of magnitude,  $r_s$  is responsible for bringing the trajectory back to the “knee area” of the  $V$ -nullsurface (slow manifold). When this region is reached,  $r_f$  and  $r_s$  evolve roughly on the same time scale and trajectories rotate around the knee until they are allowed to leave the rotation area and escape the regime. The value of  $V$  at which the escape happens, if at all, is the one corresponding the peak of a STO. Thus the canard structure approach explains why spikes occurs at the peak of the STOs, as experimentally found (Dickson et al., 2000b).

The dynamics of (4)–(6), described by the canard structure, cannot be simplified to a noisy two-dimensional linear model. As we show in Fig. 12, the time scale separation is lost in neighborhoods of stable foci, around which system (4)–(6) has to be linearized in order to see STOs. However, since foci are far away from the reset values, trajectories of the linearized system around a focus will evolve with a very large starting amplitude (almost equal to the distance between the chosen focus and the reset values); i.e., not in the STO range, reaching threshold before getting to the STO region. As a consequence of that, no STOs and MMOs will be seen. However, a noisy two-dimensional model with a canard structure can be used to produced MMOs similar to the ones shown in this paper. To achieve that,  $I_{h_s}$  has to be replaced by an increase in the value of  $I_{app}$  (constant), so the trajectory returns to the STO region.

The patterns of activity seen in experiments are very irregular, in contrast to the regular patterns (a constant number of STOs per spike) obtained in our deterministic SC model.

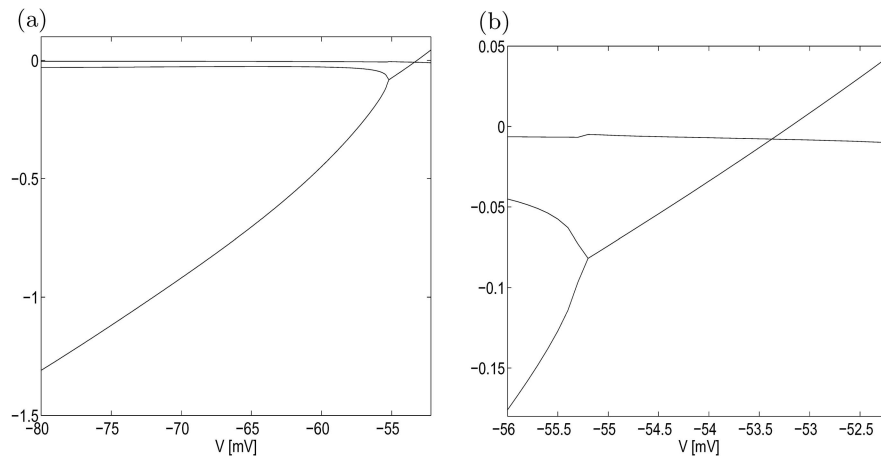


**Fig. 12** Real part of the eigenvalues for the reduced system (4)–(6) as a function of the  $V$ -coordinate of the fixed point.  $G_h = 1.5$  and the values of the other parameters are given in Section 2. The right panel is a blow up of the left one. For lower values of  $V$  the three eigenvalues have zero complex part. For the highest values of  $V$  in the figure, two of

the eigenvalues have nonzero complex part (conjugate). These values of  $V$  correspond to fixed points close to the “knee” of the slow manifold. The time scale separation decreases as the fixed point gets closer to the knee. For fixed points in the oscillatory regime, there is no time scale separation.

In terms of the canard mechanism proposed in this paper, the occurrence of a spike can be thought of as a loss of stability of the STO regime (a spiking instability). In related theoretical work, stochastic models with persistent sodium channel noise, have been successfully used to enhance the robustness of STOs (White et al., 1998). In Section 3.4 we obtained the same result for our NAS SC model and we identified conditions under which the STOs are very close to a sinusoidal function.

One explanation for the effect of noise in enhancing the robustness of STOs might be that noise suppresses spikes; i.e., noise prevents spiking by moving the  $V$ -nullcline in a way that forces the trajectory to stay away from the spiking instability. However, our theoretical approach (using the canard structure) suggests that this is not necessarily the case. For the parameters considered in our simulations, the most robust STOs are obtained when, in the absence of noise, the SC is silent but close to STO activity. The effect of noise is to force the system to move around the knee of the voltage nullcline, thus creating a STO. In this sense, noise creates an “intermediate STO state” in between silence and STO/spiking. While the trajectory is moving close to the  $V$ -nullsurface unstable branch, the effect of noise is not very important. If the noise amplitude ( $D$ ) is too big, a spike can be produced when the trajectory gets close to the knee. Otherwise, the trajectory continues to oscillate.

The structural dynamic ideas presented here are consistent with previous theoretical observations (based on simulation results) by Fransén et al. (2004). Using a noisy model, they concluded that  $I_{h_f}$ , rather than  $I_{h_s}$ , is the major factor in the oscillation generation. Our theory predicts that  $r_s$  is necessary to bring the trajectory back to the neighborhood of the “knee” of  $N(V; r_s)$  after a spike has occurred. However, once

the trajectory is there, in the noisy model, robust STOs can occur in the absence of  $r_s$ . Fransén et al. (2004) also found that, consistent with experimental results, full or partial blockade of  $I_{h_s}$  abolishes oscillations. Blockade of  $I_{h_s}$  is modeled by decreasing the value of  $G_h$ , which has the effect of moving the nullsurface  $N(V; r_s)$  up, while keeping  $r_{f,\infty}(V)$  unchanged (see Fig. 13 for the effect of changes in parameters on the canard structure). The stable fixed point  $P(0)$  is then farther away from the knee and one can find regimes in which STOs are not possible (unless  $r_s$  has a quicker time scale and lowers  $N(V; r_s)$  in a timely manner).

As in Fransén et al. (2004), the  $I_{h_s}$  gating variable time scales ( $\tau_{r_f}$  and  $\tau_{r_s}$ ) are voltage dependent. Models with time-independent time scales have been proposed (Spain et al., 1987; Richardson et al., 2003; Schreiber et al., 2004). Their values and the ones we use here in the STO regime have approximately the same order of magnitude. From the dynamic point of view, voltage-independent time scale models differ from voltage dependent ones in that  $I_{h_s}$  does not reset during a spike. Consequently, the initial conditions for  $r_f$  and  $r_s$  in the STO regime are not necessarily zero. If they are high enough, the trajectories may escape the spiking regime without performing STOs, as we show in Fig. 14. (In the Figure  $r_f(0) \neq 0$  and  $r_s = 0$ , but the same type of picture can be obtained for  $r_f(0) = 0$  if  $r_s(0) \neq 0$  is high enough). In this case, even though STOs are not observed, the system has the potential of producing them. They might be uncovered by different types of external inputs (synaptic or sinusoidal) in network and resonance studies.

Clustering, MMOs in which two or more consecutive spikes come in a row with no STOs in between, is a pattern seen in SCs. Fransén et al. (2004) found clustering patterns by performing simulations in a model with additional

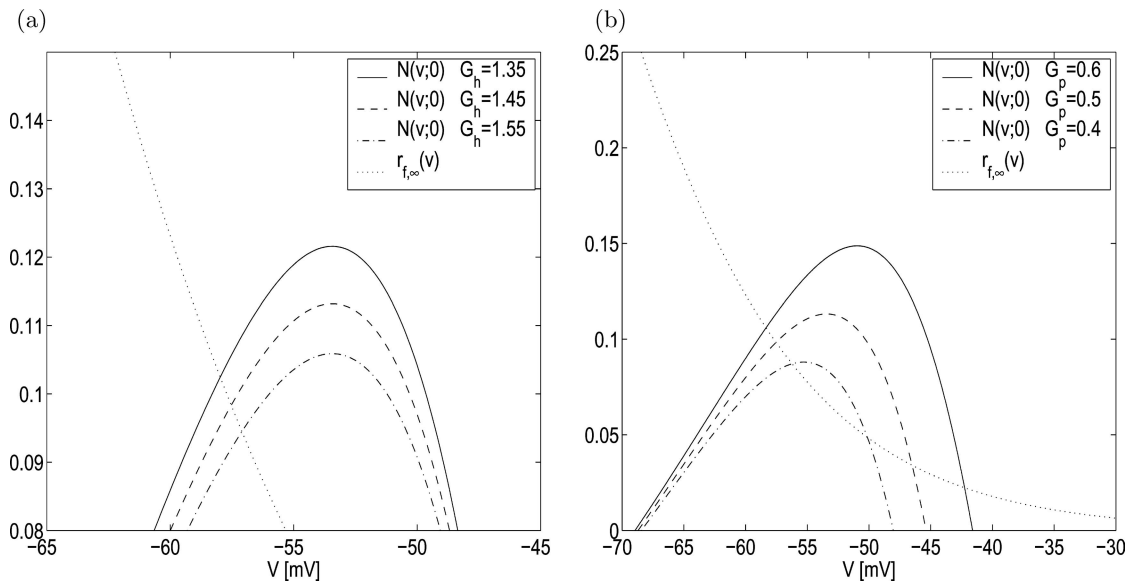


**Fig. 13** Changes in the parameters of the model are reflected in the properties of the canard structure. Here, the  $V$ -nullsurfaces are represented by the nullclines  $N(V; 0)$  (the projections of the  $V$ -nullsurfaces onto the plane  $r_s = 0$ ). Increasing the value of  $G_h$  or  $G_p$  and keeping all

other parameters constant moves the  $V$ -nullsurfaces down and makes it easier for the cell to fire. The values of the parameters, except  $G_p$  and  $G_h$ , are given in Section 2. (a)  $G_p = 0.5$ . (b)  $G_h = 1.45$ .

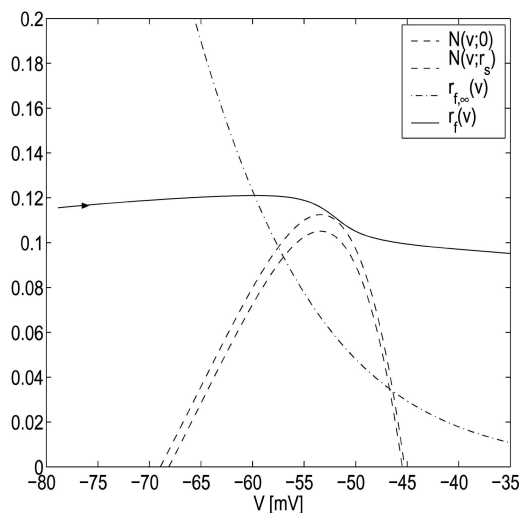


**Fig. 14** STOs may not be observed if  $I_h$  does not reset. The values of the parameters are as in Fig. 6 ( $G_h = 1.5$  and  $I_{app} = -2.5$  and the value of the other parameters used in the simulations are given in Section 2). The initial conditions for  $r_f$  is  $r_f(0) = 0.115$  (different from the reset value  $r_f(0) = 0$ ). The initial conditions for  $V$  and  $r_s$  are as in Fig. 6.  $N(V; 0)$  and  $N(V; r_s)$  are the upper and lower  $V$ -nullclines respectively. The latter was calculated for an approximation of the highest value of  $r_s$ . When the trajectory (for  $r_f$  and  $V$  when  $r_s$  evolves continuously) reaches the “knee” area,  $N(V; r_s)$  has moved down enough (to an intermediate curve between the two shown in the figure) so the trajectory escapes the regime without displaying STOs.

currents. They found that  $I_h$  (specially its slow component) plays an important role in clustering. The reset of  $I_h$  in the current paper prevents clustering from occurring in the model

studied in this paper since, after each spike, the initial conditions in the STO regime force the trajectory to perform at least one STO before being able to escape to the spiking regime. However, the underlying canard structure gives some hints on possible and biologically plausible clustering mechanisms. Assuming a reduced regime like the STO regime presented in this manuscript, one hypothetical mechanism would include an extra current that could be a modulatory current in the STO regime or an active current in the intermediate regime (in between the spiking and the STO one that governs the recovery of the SC after a spike). The role of this current would be to make  $r_f$  and  $r_s$  evolve from their reset values to values that are high enough to escape the STO regime without performing any STOs. A second hypothetical mechanism involves the nullsurface geometry instead of initial (reset) conditions; it would include an extra current whose role is to transiently moves the nullsurface  $N(V; r_s)$  downwards, thus allowing the trajectory to escape the regime without performing STOs. This current may or may not be modulatory. In the latter case, the dimensionality of the STO regime would be increased.

The function of STOs is not clear yet, but they are believed by some to play a role in synchronization and other coherent dynamic behavior (Hutcheon and Yarom, 2000; Dickson et al., 2000a; Buzsáki and Draguhn, 2004). The synchronization of SCs and networks including SCs have been studied by various authors (Acker et al., 2003; Netoff et al., 2004; Rotstein et al., 2005b; Pervouchine et al., 2005). We compared the synchronization properties of SCs and networks including SC using the reduced NAS and the full SC models (see

Appendix B and Fig. 15). We found a qualitative agreement between the results in the two cases. This suggests that the relevant currents governing the synchronization properties in SCs are not the spiking currents but the ones active during the STO regime. The mechanism uncovered in this paper

is not the only possible one for STOs involving  $I_{\text{Nap}}$  and  $I_h$ . In fact, in a model for STOs in relay thalamic neurons (Izhikevich, 2005), the  $V$ -nullcline is cubic-like and intersects the  $h$ -current “gating variable nullcline” in the middle of the unstable branch (creating an unstable fixed point). STOs

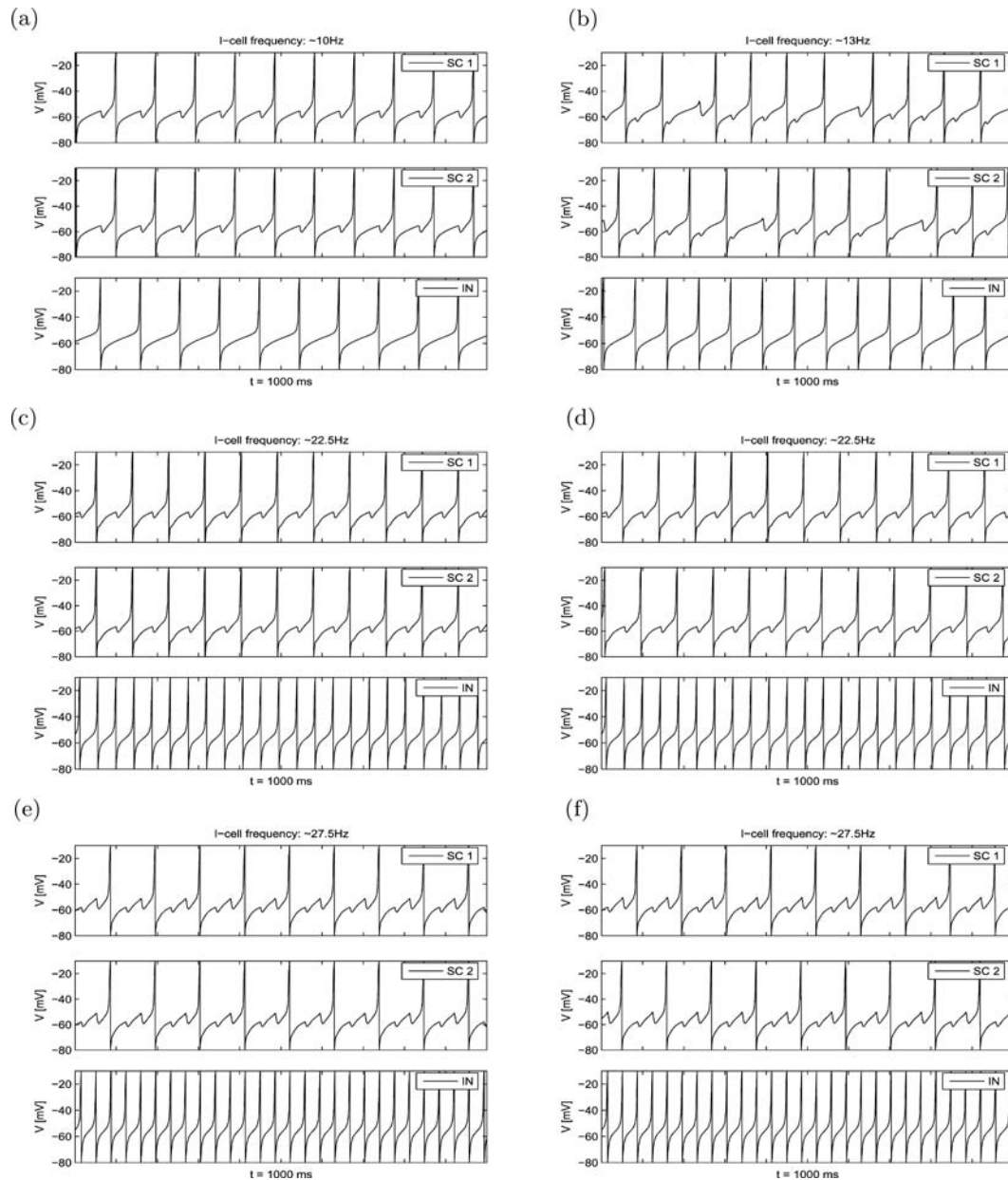


**Fig. 15** Results of simulations for two uncoupled SCs receiving GABAergic input from an interneuron at various frequencies. The synaptic function is given by (A.2) with  $\tau_1 = 5$ ,  $\tau_2 = 1.68$  ( $\tau_{\text{dec}} 6.96$ ) and  $G_s = 0.1$ . The natural frequency of the SCs is 10 Hz. The natural frequency of the I-cells ( $\nu_I$ ) is varied and displayed above each plot. As this natural frequency increases different temporal patterns are obtained. (a)  $\nu_I \sim 10$  Hz: The SCs fire in phase and the I-cell imposes its frequency to the SCs. The results are similar for  $\nu_I$  in the theta range (8–12 Hz). (b)  $\nu_I \sim 13$  Hz: The patterns are not coherent. The I-cell input is fast enough to suppress some of the SC spikes. The timing of the SCs firing is such that an input from the I-cell may advance the

spiking of one of the SCs and delay the other. (c) and (d)  $\nu_I \sim 22.5$  Hz: Depending on initial conditions the SCs fire in phase or in antiphase. The I-cell fires fast enough to suppress some of the spikes. (e) and (f)  $\nu_I \sim 27.5$  Hz: Depending on initial conditions the SCs fire in phase or with a phase lag of one third. The I-cell fires fast enough to suppress some of the spikes, but an increase of the  $h$ -current from cycle to cycle causes the SCs to fire. (g)  $\nu_I \sim 39$  Hz: It takes an increasing number of cycles for the  $h$ -current to build up enough to overcome inhibition. (h)  $\nu_I \sim 42$  Hz: The SC firing is completely suppressed. The  $h$ -current is not able to increase to high enough values as to allow the SC voltage to reach threshold (Continued on next page).

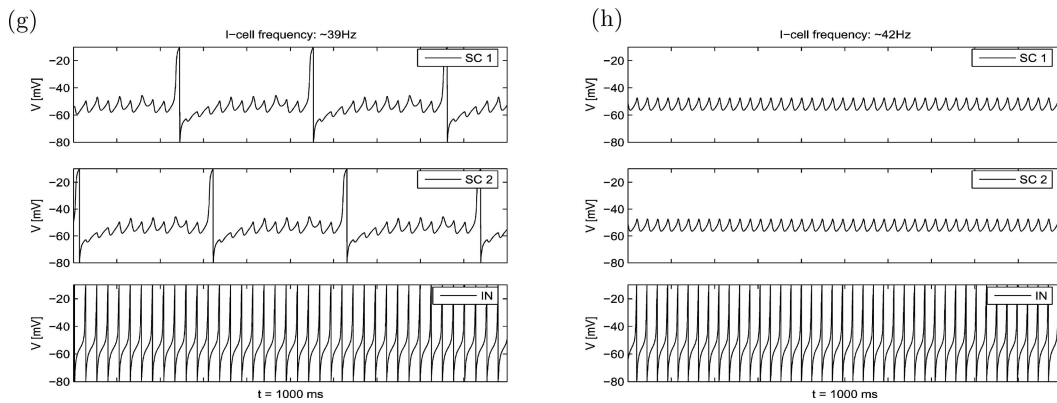


**Fig. 15** (Continued).

in that model are the result of trajectories moving around the two stable branches of the  $V$ -nullcline (Izhikevich, 2005). We hypothesize that the canard structure (as opposed to the STOs themselves) plays an important role in synchronization properties.

Problems with similar mathematical structure as the one given by Eqs. (4)–(6) have been studied by Wechselberger (2005) and Drover et al. (2004) in order to explain the spike-frequency reduction of a Hodgkin-Huxley neuron due to excitatory synaptic self-coupling. In both cases, a two-dimensional system with fast ( $V$ ) and slow ( $h$ ) variables was used to model the dynamics of the neuron, and an extra slow variable was used for an autapse on the neuron. In both cases, the reduction of spiking frequency is the result of the trajectory being trapped in a neighborhood of a fold line ( $L$  in our notation). As in our model, STOs (or MMOs) are observed in a neighborhood of  $L$ . However, in the SC model, the STOs are intrinsically generated by the single cell with no need of a synaptic self-coupling.

In this work we give heuristic arguments to explain the generation of STOs in the SC model. Work in progress, including the development of reduction of dimension techniques (Rotstein et al., 2005a) and the application of the theory developed by Wechselberger (2005), aims to make the justifications of the reductions to the NAS model and the generation of STOs more precise.

**Appendix A**

Here we give the definitions of the functions defining  $x_\infty(V)$  and  $\tau_x(V)$  :

$$\alpha_m(V) = -0.1(V + 23)/(e^{-0.1(V+23)} - 1),$$

$$\beta_m(V) = 4e^{-(V+48)/18},$$

$$\alpha_h(V) = 0.07e^{-(V+37)/20},$$

$$\beta_h(V) = 1/(e^{-0.1(V+7)} + 1),$$

$$\alpha_n(V) = -0.01(V + 27)/(e^{-0.1(V+27)} - 1),$$

$$\beta_n(V) = 0.125e^{-(V+37)/80},$$

$$\alpha_p(V) = 1/(0.15(1 + e^{-(V+38)/6.5})),$$

$$\beta_p(V) = e^{-(V+38)/6.5}/(0.15(1 + e^{-(V+38)/6.5})),$$

$$r_{f,\infty}(V) = 1/(1 + e^{(V+79.2)/9.78}),$$

$$\tau_{r_f}(V) = 0.51/(e^{(V-1.7)/10} + e^{-(V+340)/52}) + 1,$$

$$r_{s,\infty}(V) = 1/(1 + e^{(V+2.83)/15.9})^{58},$$

$$\tau_{r_s}(V) = 5.6/(e^{(V-1.7)/14} + e^{-(V+260)/43}) + 1.$$

Note that  $\tau_p(V) = 0.15$  and  $p_\infty(V) = 1/(1 + e^{-(V+38)/6.5})$ . The function  $r_{s,\infty}(V)$  used here differs from the one published in Acker et al. (2003):  $r_{s,\infty} = 1/(1 + e^{(V+71.3)/7.9})$ . The former corresponds to an earlier version of that paper. Both forms are almost equal, specially in the STI.

**Appendix B: Synchronization properties of networks of NAS SC models**

The full SC model (1)–(3) has been used to explain the role of  $I_h$  in the synchronization properties of networks including SCs and other cells having similar electric properties

(Acker et al., 2003; Netoff et al., 2004; Jalics et al., 2004; Rotstein et al., 2005b). Among the latter we mention the oriens lacunosum-moleculare (O-LM) cells in the hippocampus (Gillies et al., 2002). In previous sections we showed that the effects of  $I_h$  are captured by the NAS SC model (4)–(6). As a way of further checking its validity, here we study the synchronization properties of networks models, including the NAS SC model. We compare our results with previous ones using the full SC model.

To consider the effect of synaptic currents to each SC we add a synaptic term  $-I_S$  to the current-balance Eq. (4)

$$C \frac{dV}{dt} = I_{\text{app}} - G_p p_{\infty}(V)(V - E_{Na}) - I_L - I_h - I_S \quad (\text{A.1})$$

where  $I_S = G_S S(v - E_{\text{rev}})$  and  $E_{\text{rev}} = E_{\text{ex}} = 0$  mV or  $E_{\text{rev}} = E_{\text{in}} = -80$  mV (corresponding to  $\text{GABA}_A$ , for excitatory or inhibitory synaptic connections respectively). The synaptic variable  $S$  we used is given by Dayan and Abbott (2001)

$$S = S_N (e^{-t/\tau_1} - e^{-t/\tau_2}), \quad \text{with} \\ S_N = \left[ \left( \frac{\tau_2}{\tau_1} \right)^{\tau_{\text{rise}}/\tau_1} - \left( \frac{\tau_2}{\tau_1} \right)^{\tau_{\text{rise}}/\tau_2} \right]^{-1}. \quad (\text{A.2})$$

We define the decay time  $\tau_{\text{dec}}$  as the time it takes  $S$  to decay from its maximum value to 0.37 % ( $1/e$ ) of its maximum value. Below, the units of  $\tau_1$ ,  $\tau_2$  and  $\tau_{\text{dec}}$  are msec, and the units of  $G_S$  are  $\text{mS}/\text{cm}^2$ . We performed simulations for different natural frequencies of the SCs in the theta range (8–12 Hz). The natural frequency of a cell is its firing frequency when uncoupled.

We consider different types of networks in which excitatory and/or inhibitory connections are present. SCs are excitatory and they are connected via AMPA. The full SC model has been used for O-LM cells in the hippocampus (Rotstein et al., 2005b). In contrast to the SCs, O-LM cells are inhibitory, mediated by  $\text{GABA}_A$ . We used various kinetics for both AMPA and  $\text{GABA}_A$ , summarized in Table 1. The  $\text{AMPA}^1$  and  $\text{AMPA}^2$  kinetics have been considered by Acker et al. (2003) and Netoff et al. (2004) respectively. The  $\text{GABA}_A^1$  kinetics has been considered by Netoff et al. (2004). The  $\text{GABA}_A^2$  kinetics is standard (Destexhe et al., 1994; Dayan and Abbott, 2001) but has not been used in networks including SCs. The  $\text{GABA}_A^3$  and  $\text{GABA}_A^4$  kinetics correspond to values used by Rotstein et al. (2005b) for O-LM cells.

For two SCs connected via  $\text{AMPA}^1$  and  $\text{AMPA}^2$  our results are consistent with the findings by Acker et al. (2003) using the full SC model. For two SCs connected via  $\text{GABA}_A^4$

**Table 1** Parameters and decay times ( $\tau_{\text{dec}}$ ) for synaptic connections of various kinetic types (AMPA and  $\text{GABA}_A$ ). The units of  $\tau_1$ ,  $\tau_2$  and  $\tau_{\text{dec}}$  are msec.

Synapse type	$\tau_{\text{dec}}$	$\tau_1$	$\tau_2$
$\text{AMPA}^1$	6.15	5.30	0.78
$\text{AMPA}^2$	8.13	6.21	1.68
$\text{GABA}_A^1$	6.96	5.00	1.68
$\text{GABA}_A^2$	5.92	5.60	0.28
$\text{GABA}_A^3$	10.00	9.70	0.30
$\text{GABA}_A^4$	20.00	19.70	0.30

kinetics (the four cases shown in Table 1) the results are consistent with the findings by Netoff et al. (2003), Rotstein et al. (2005b) using the full SC model. In both cases the natural frequencies was in the theta range (8–12 Hz).

To study the effect of common inhibition on two uncoupled SCs we connect an interneuron (I-cell), using a standard Hodgkin-Huxley model, to the two SCs using  $\text{GABA}_A^1$  synaptic connections (see Table 1) as in the experiments using hybrid networks (*in vitro* and *in silico*) by Netoff et al. (2004). The I-cell is set to fire rhythmically over a large range of frequencies (from 8 up to  $\sim 60$  Hz). The natural frequency of the SC is 10 Hz and  $G_s = 0.1$ .

Our results are summarized in Fig. 15. They are qualitatively similar to the results performed using the full SC model where, in contrast to our current case, the two SCs were coupled via inhibition (Rotstein et al., 2005b).

**Acknowledgments** The authors thank Angel Alonso for critically reading an earlier version of the paper and for making very useful comments and suggestions. Thanks also go to Andreas Herz, Martin Wechselberger, Martin Krupa, Steve Epstein and Carson Chow for fruitful discussions.

This work was partially supported by the Burroughs Wellcome Fund (HGR), NIH grant 5 RO1 NS46058 (NK), NSF grant DMS-0211505 (NK) and the graduate program “Dynamics and Evolution of Cellular and Macromolecular Processes” of the German Research Foundation, DFG (TO).

## References

- Acker CD, Kopell N, White JA (2003) Synchronization of strongly coupled excitatory neurons: Relating network behavior to biophysics. *J. Comput. Neurosci.* 15: 71–90.
- Alonso AA, García Austt E (1987) Neuronal sources of theta rhythm in the entorhinal cortex of the rat. II. Phase relations between unit discharges and theta field potentials. *Exp. Brain Res.* 67: 493–501.
- Alonso AA, Klink R (1993) Differential electroresponsiveness of stellate and pyramidal-like cells of medial entorhinal cortex layer II. *J. Neurophysiol.* 70: 144–157.
- Alonso AA, Llinás RR (1989) Subthreshold  $\text{Na}^+$ -dependent theta like rhythmicity in stellate cells of entorhinal cortex layer II. *Nature* 342: 175–177.
- Baer SM, Erneux T, Rinzel J (1989) The slow passage through a Hopf bifurcation: delay, memory effects, and resonance. *SIAM J. Appl. Math.* 49: 55–71.

- Benoit E, Callot JL, Diener F, MD (1980) Chasse au Canard. IRMA, Strasbourg.
- Brons M, Krupa M, Wechselberger M (2005) Mixed mode oscillations due to the generalized canard phenomenon. Submitted.
- Burden RL, Faires JD (1980) Numerical Analysis. PWS Publishing Company, Boston.
- Buzsáki G (1989) Two-stage model of memory trace formation: A role for 'noisy' brain states. *Neuroscience* 31: 551–570.
- Buzsáki G, Draguhn (2004) Neuronal oscillations in cortical networks. *Science* 304: 1926–1929.
- Chow CC, White JA (1996) Spontaneous action potentials due to channel fluctuation. *Biophys. J.* 71: 3013–3021.
- Clewley R, Rotstein HG, Kopell N (2005) A computational tool for the reduction of nonlinear ode systems possessing multiple scales. *SIAM J. Multiscale Model. Sim.* (in press).
- Dayan P, Abbott LF (2001) Theoretical Neuroscience. The MIT Press.
- Destexhe A, Mainen ZF, Sejnowski TJ (1994) Synthesis of models for excitable membranes, synaptic transmission and neuromodulation using a common kinetic formalism 3: 195–230.
- Dickson CT, Magistretti J, Shalinsky M, Hamam B, Alonso AA (2000a) Oscillatory activity in entorhinal neurons and circuits. *Ann. NY Acad. Sci.* 911: 127–150.
- Dickson CT, Magistretti J, Shalinsky MH, Fransén E, Hasselmo M, Alonso AA (2000b) Properties and role of  $I_h$  in the pacing of subthreshold oscillation in entorhinal cortex layer II neurons. *J. Neurophysiol.* 83: 2562–2579.
- Drover J, Rubin J, Su J, Ermentrout B (2004) Analysis of a canard mechanism by which excitatory synaptic coupling can synchronize neurons at low firing frequencies. *SIAM J. Appl. Math.* 65: 69–92.
- Dumortier F, Roussarie R (1996) Canard cycles and center manifolds. *Mem. Am. Math. Soc.* 121 (577).
- Eckhaus W (1983) Relaxation oscillations including a standard chase on french ducks. In *Lecture Notes in Mathematics*, Springer-Verlag 985: 449–497.
- Erchova I, Kreck G, Heinemann U, Herz AVM (2004) Dynamics of rat entorhinal cortex layer II and III cells: characteristics of membrane potential resonance at rest predict oscillation properties near threshold. *J. Physiol.* 560: 89–110.
- Fenichel N (1971) Persistence and smoothness of invariant manifolds for flows. *Ind. Univ. Math. J.* 21: 193–225.
- Fransén E, Alonso AA, Dickson CT, Magistretti J, Hasselmo ME (2004) Ionic mechanisms in the generation of subthreshold oscillations and action potential clustering in entorhinal layer II stellate neurons. *Hippocampus* 14: 368–384.
- Fransén E, Dickson CT, Magistretti J, Alonso AA, Hasselmo ME (1998) Modeling the generation of subthreshold membrane potential oscillations of entorhinal cortex layer II stellate cells. *Soc. Neurosci. Abstr.* 24: 814–815.
- Fransén E, Wallestein GV, Alonso AA, Dickson CT, Hasselmo ME (1999) A biophysical simulation of intrinsic and network properties of entorhinal cortex. *Neurocomputing* 26–27: 375–380.
- Gillies MJ, Traub RD, LeBeau FEN, Davies CH, Gloveli T, Buhl EH, Whittington MA (2002) A model of atropine-resistant theta oscillations in rat hippocampal area CA1. *J. Physiol.* 543.3: 779–793.
- Hutcheon B, Miura RM, Puil E (1996) Subthreshold membrane resonance in neocortical neurons. *J. Neurophysiol.* 76: 683–697.
- Hutcheon B, Yarom Y (2000) Resonance oscillations and the intrinsic frequency preferences in neurons. *Trends Neurosci.* 23: 216–222.
- Izhikevich E (2005) Dynamical Systems in Neuroscience. (<http://www.nsi.edu/users/izhikevich/publications/index.htm>), Section 5.1.4. MIT Press.
- Izhikevich EM (2001) Resonate-and-fire neurons. *Neural Netw.* 14: 883–894.
- Jalics J, Kispersky T, Dickson C, Kopell N (2004) Neuronal ensembles and modules: Modeling dynamics in medial entorhinal cortex. *Soc. Neurosci. Abstr.* 517.1.
- Jalics J, Rotstein HG, Kopell N (2005) Unpublished data.
- Kahana MJ, Sekuler R, Caplan JB, Kirschen M, Madsen JR (1999) Human theta oscillations exhibit task dependence during virtual maze navigation. *Nature* 399: 781–784.
- Klink RM, Alonso A (1993) Ionic mechanisms for the subthreshold oscillations and differential electroresponsiveness of medial entorhinal cortex layer II neurons. *J. Neurophysiol.* 70: 128–143.
- Klink RM, Alonso AA (1997) Ionic mechanisms of muscarinic depolarization in entorhinal cortex layer II neurons. *J. Neurophysiol.* 77: 1829–1843.
- Koch C (1999) Biophysics of Computation. Oxford University Press.
- Kopell N, LeMasson G (1994) Rhythmogenesis, amplitude modulation, and multiplexing in a cortical architecture. *Proc. Natl. Acad. Sci. USA* 91: 10586–10590.
- Krupa M, Szmolyan P (2001) Relaxation oscillation and canard explosion. *J. Diff. Eq.* 174: 312–368.
- Llinás RR, Yarom Y (1981) Electrophysiology of mammalian inferior olivary neurons *in vitro* different types of voltage-dependent ionic conductances. *J. Physiol.* 315: 549–567.
- Llinás RR, Yarom Y (1986) Oscillatory properties of guinea pig olivary neurons and their pharmacological modulation: An *in vitro* study. *J. Physiol.* 376: 163–182.
- Magistretti J, Alonso AA (1999) Biophysical properties and slow voltage-dependent inactivation of a sustained sodium current in entorhinal cortex layer-II principal neurons. a whole-cell and single-channel study. *J. Gen. Physiol.* 114(4): 491–509.
- Magistretti J, Ragsdale DS (1999) High conductance sustained single-channel activity responsible for the low-threshold persistent  $Na^+$  current in entorhinal cortex neurons. *J. Neurosci.* 19(17): 7334–7341.
- Makarov VA, Nekorkin VI, Velarde MG (2001) Spiking behavior in a noise-driven system combining oscillatory and excitatory properties. *Phys. Rev. Lett.* 15: 3031–3034.
- Neishtadt AI (1987) Persistence of stability loss for dynamical bifurcations I. *Diff. Eqs.* 23: 1385–1391.
- Neishtadt AI (1988) Persistence of stability loss for dynamical bifurcations II. *Diff. Eqs.* 24: 171–176.
- Netoff T, Banks M, White J (2003) Bridging single cell and network dynamics. *Soc. Neurosci. Abstr.* 32: 171.7.
- Netoff T, Pervouchine D, Kopell N, White J (2004) Oscillation frequency switches in model and hybrid networks of the hippocampus. *Soc. Neurosci. Abstr.* \*32\*. In press.
- Pervouchine DD, Netoff TI, Rotstein HG, White JA, Kopell N (2005) Low-dimensional maps encoding dynamics in entorhinal cortex and hippocampus. In revision.
- Richardson MJE, Brunel N, Hakim V (2003) From subthreshold to firing-rate resonance. *J. Neurophysiol.* 89: 2538–2554.
- Rinzel J (1985) Excitation dynamics: Insights from simplified membrane models. *Fed. Proc.* 44: 2944–2946.
- Rotstein HG, Clewley R, Wechselberger M, Kopell N (2005a) Reduction of dimensions and dynamics of a medial entorhinal cortex layer II stellate cell model. In preparation.
- Rotstein HG, Pervouchine D, Gillies MJ, Acker CD, White JA, Buhl EH, Whittington MA, Kopell N (2005b) Slow and fast inhibition and  $h$ -current interact to create a theta rhythm in a model of CA1 interneuron networks. *J. Neurophysiol.* 94: 1509–1518.
- Schreiber S, Erchova I, Heinemann U, Herz AV (2004) Subthreshold resonance explains the frequency-dependent integration of periodic as well as random stimuli in the entorhinal cortex. *J. Neurophysiol.* 92: 408–415.
- Shalinsky JH, Magistretti J, Ma L, Alonso AA (2002) Muscarinic activation of a cation current and associated current noise

- in entorhinal-cortex layer-II neurons. *J. Neurophysiol.* 88: 1197–1211.
- Spain WJ, Schwindt PC, Crill WE (1987) Anomalous rectification in neurons from cat sensorimotor cortex *in vitro*. *J. Neurophysiol.* 57: 1555–1576.
- Szmolyan P, Wechselberger M (2001) Canards in  $R^3$ . *J. Diff. Eq.* 177: 419–453.
- Wechselberger M (2005) Existence and bifurcation of canards in  $R^3$  in the case of a folded node. *SIAM J. Appl. Dyn. Syst.* 4: 101–139.
- White JA, Budde T, Kay ARA (1995) A bifurcation analysis of neuronal subthreshold oscillations. *Biophysical. J.* 69: 1203–1217.
- White JA, Klink R, Alonso A, Kay ARA (1998) Noise from voltage-gated ion channels may influence neuronal dynamics in the entorhinal cortex. *J. Neurophysiol.* 80: 262–269.
- White JA, Rubinstein JT, Kay AA (2000) Channel noise in neurons. *Trends Neurosci.* 23(3): 131–137.
- Winson J (1978) Loss of hippocampal theta rhythm results in spatial memory deficit in the rat. *Science* 201: 160–163.